


# Boundary-obstructed topological superconductor in buckled honeycomb lattice under perpendicular electric field

Rasoul Ghadimi , Seung Hun Lee, and Bohm-Jung Yang\*

*Center for Correlated Electron Systems, Institute for Basic Science (IBS), Seoul 08826, Korea;*

*Department of Physics and Astronomy, Seoul National University, Seoul 08826, Korea;*

*and Center for Theoretical Physics (CTP), Seoul National University, Seoul 08826, Korea*



(Received 6 March 2023; revised 5 June 2023; accepted 6 June 2023; published 15 June 2023)

In this work, we show that a buckled honeycomb lattice can host a boundary-obstructed topological superconductor (BOTS) in the presence of  $f$ -wave spin-triplet pairing (fSTP). The underlying buckled structure allows for the manipulation of both chemical potential and sublattice potential using a double gate setup. Although a finite sublattice potential can stabilize the fSTP with a possible higher-order band topology, because it also breaks the relevant symmetry, the stability of the corner modes is not guaranteed. Here we show that the fSTP on the honeycomb lattice gives a BOTS under nonzero sublattice potential, thus the corner modes can survive as long as the boundary is gapped. Also, by examining the large sublattice potential limit where the honeycomb lattice can be decomposed into two triangular lattices, we show that the boundary modes in the normal state are the quintessential ingredient leading to the BOTS. Thus the effective boundary Hamiltonian becomes nothing but the Hamiltonian for Kitaev chains, which eventually gives the corner modes of the BOTS.

DOI: [10.1103/PhysRevB.107.224511](https://doi.org/10.1103/PhysRevB.107.224511)

## I. INTRODUCTION

Although superconductivity has not yet been observed in pristine graphene, it has been experimentally realized in related families such as multilayer [1–3], twisted moiré bilayer [4], and alkali-metal intercalated graphene [5–9]. Remarkably, underlying symmetries of the honeycomb lattice allow the emergence of various topologically nontrivial states, such as chiral  $p$ -wave and  $d$ -wave pairings [10–21]. Recently, it has been shown that the  $f$ -wave spin-triplet pairing (fSTP) [10,22–37] can arise in the honeycomb lattice, deriving higher-order topological superconductivity (HOTS) [38,39] that hosts zero-energy Majorana corner modes, protected by both bulk gap and certain spatial symmetries, such as inversion symmetry [40–52]. Also, fSTP was shown to be enhanced when there is a large sublattice potential [53,54]. For instance, an electric field perpendicular to the plane of a low-buckled honeycomb lattice such as silicene can induce a considerable sublattice potential and stabilize fSTP [see Figs. 1(b) and 1(c)] [55]. However, as the sublattice potential breaks the essential symmetries that protect HOTS simultaneously, the stability of the corner modes is not guaranteed unless a distinct mechanism for their intrinsic protection exists.

In this paper, we show that fSTP can host corner modes that remain intact even under a considerable sublattice potential. Interestingly, the sublattice potential turns the HOTS into an extrinsic topological superconductor [40,41,56–68] or a boundary obstructed topological superconductor (BOTS) [69–76], where corner modes are protected by the energy gap of the edge Hamiltonian, not the bulk Hamiltonian. We also

propose a double gate setup that enables the realization of a tunable BOTS phase transition.

In the following, we first illustrate how unbroken symmetries can protect the BOTS phase, and then we analyze the large sublattice potential limit of honeycomb lattices, which effectively can be mapped into two triangular lattices. We demonstrate that the existence of boundary modes in the normal state (without superconductivity) is crucial for the BOTS (in the superconducting state). As fSTP acts effectively as a  $p$ -wave pairing for these boundary modes, the corner modes in the BOTS can be interpreted as the end modes of Kitaev chains [77] on the boundaries.

The rest of the paper is organized as follows. In Sec. II, we introduce our model to study fSTP in a honeycomb lattice. Then in Sec. III, we describe the boundary-obstructed topological nature of the model and show its relation to the topological physics of the Kitaev chain. In Sec. IV, we give a brief discussion on the disorder, interaction, and extension of BOTS to spin-polarized cases. Finally, we summarize our results in Sec. V.

## II. MODEL

The Bogoliubov–de Gennes (BdG) Hamiltonian for the honeycomb lattice with  $p_z$  orbital and fSTP is given by (see Appendix A for a derivation)

$$H_{\text{BdG}}(\mathbf{k}) = t_1 H_1^{++}(\mathbf{k})\sigma_x\tau_z + t_1 H_1^{-+}(\mathbf{k})\sigma_y\tau_z + t_2 H_2^{++}(\mathbf{k})\tau_z - \mu\tau_z + M\sigma_z\tau_z + \Delta_s H_3^{+-}(\mathbf{k})s_x\tau_y, \quad (1)$$

where  $t_1$ ,  $t_2$ ,  $\mu$ , and  $M$  are nearest-neighbor hopping, next-nearest-neighbor hopping, chemical potential, and sublattice potential, respectively [78,79]. We note that  $\mu$  and  $M$  can be changed by controlling the gate voltage [see Fig. 1(b)].

\*bjyang@snu.ac.kr

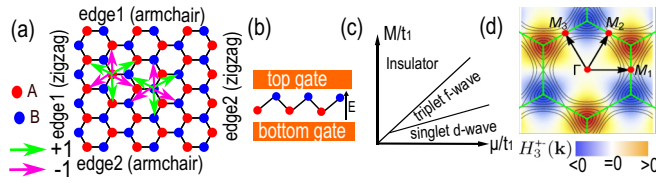


FIG. 1. The fSTP in the honeycomb lattice. (a) The top view of the honeycomb lattice with fSTP between next-nearest-neighbor sites (shown with arrows). (b) Double gate setup for tuning both  $\mu$  and  $M$  in a buckled honeycomb lattice. (c) The schematic superconducting phase diagram of a honeycomb lattice proposed in [55]. (d) Momentum space distribution of a general fSTP [ $H_3^{\pm}(\mathbf{k})$  in Eq. (1)].

In Eq. (1),  $\sigma_{x,y,z}$ ,  $s_{x,y,z}$ ,  $\tau_{x,y,z}$  are the Pauli matrices for sublattice, spin, and electron-hole degrees of freedom. The  $H_n^{\eta_1, \eta_2}(k_x, k_y)$  are momentum-dependent functions, in which  $H_n^{\eta_1, \eta_2}(k_x, k_y) = \eta_1 H_n^{\eta_1, \eta_2}(-k_x, k_y)$ ,  $H_n^{\eta_1, \eta_2}(k_x, k_y) = \eta_2 H_n^{\eta_1, \eta_2}(k_x, -k_y)$ , and their explicit forms are provided in Appendix A. In Eq. (1),  $\Delta_s = (\Delta_A + \Delta_B)/2$  is the sublattice symmetric amplitude of fSTP, where  $\Delta_A$  and  $\Delta_B$  are the amplitude of fSTP on  $A$  and  $B$  sublattices, respectively. The  $H_3^{\pm}(\mathbf{k})$  in Eq. (1) is the Fourier transform of fSTP in real space [see the arrows in Fig. 1(a)], in which its zeros (pairing nodes) are located along  $\Gamma - M_{1,2,3}$  [see Fig. 1(d)]. In this paper, we are interested in a low doping limit in which the fSTP always gives a fully gapped superconductor to

distinguish the in-gap corner modes. In the following, to investigate the topological state of Eq. (1), we suppose a nonzero fSTP regardless of  $\mu$  and  $M$ .

### III. RESULTS

We summarize the topological characteristic of Eq. (1) in the last row of Fig. 2. In Fig. 2(a), we show that when  $\mu = M = 0$  (we set  $t_2 = 0$  for simplicity), the system hosts gapless states for all boundaries. In Fig. 2(b), we turn on  $\mu \neq 0$  and set  $M = 0$ . In this case, the gapless edge modes still exist along the armchair edges [Fig. 2(b4)] and the top and bottom edges of Fig. 2(b2)]. Here, the system is a topological crystalline superconductor, where  $\mathcal{C}_{2y}: (x, z) \rightarrow -(x, z)$  symmetric edges (armchair edges) remain gapless. In the absence of these symmetric edges, the system is HOTS [see Fig. 3(f)], which was already discussed in Ref. [39]. The HOTS arises from the fact that certain symmetry operators (e.g., inversion) flip the gap sign on the edge Hamiltonian, which gives in-gap states, called corner modes. In Fig. 2(c) we set  $0 < |M| < |\mu|$ . In this case, although no gapless one-dimensional (1D) edge mode remains for the system, zero-energy corner modes still appear. Note that depending on the signs of  $M$  and  $\mu$ , the corner modes appear at different edges. We will show that this phase is a BOTS. The BOTS is protected by mirror  $\mathcal{M}_y: y \rightarrow -y$  symmetry, and corner modes survive as long as  $\mathcal{M}_y$  symmetric edges (zigzag edges) remain gapped. In Figs. 2(d) and 2(e), we show that corner modes can be eliminated via

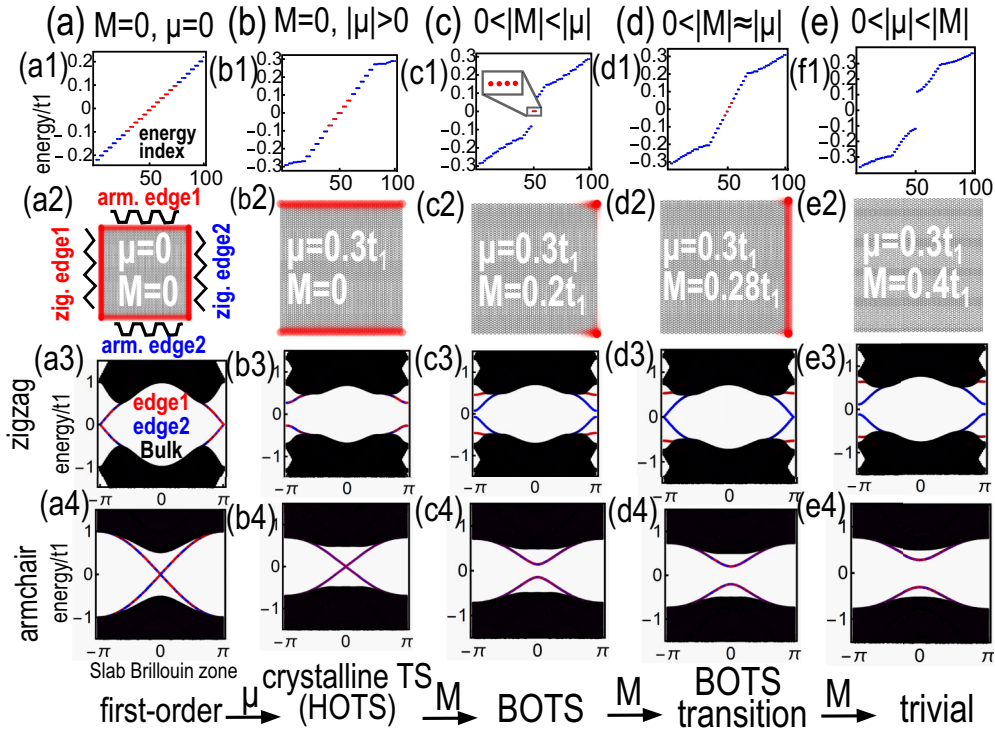


FIG. 2. Sequence of topological phase transitions by varying  $\mu$  and  $M$ . In the first row, we plot the energy spectrum for the square geometry given in the second row. In the second row, we plot the local density of states with red dots for the energy states indicated by red in the first row. In the third and fourth rows, we plot the energy spectrum for the zigzag and armchair strip geometries, respectively, with translational invariance along one direction where we show the probability of the wave function on the bulk and two edges [see Fig. 2(a2)] by black and red/blue colors. In these figures, we set  $t_2 = 0$ ,  $\Delta_s = 0.1t_1$ , and  $\mu$  and  $M$  written inside the second row of each column.

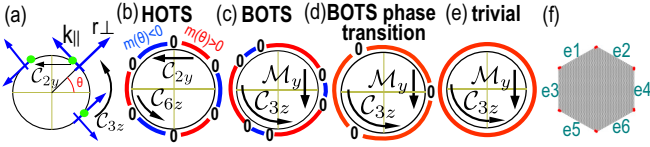


FIG. 3. (a) Disk geometry for edge theory. (b)–(e) Schematic plot of the edge mass sign for the edge Hamiltonian in different topological phases. (b) In HOTS, certain symmetry operators such as  $C_{2y}$ ,  $C_{6z}$  force mass sign changing for different edges, and zero-edge mass for symmetric edges. (c) In BOTS, the remaining spatial symmetries such as  $M_y$ ,  $C_{3z}$  do not enforce mass sign reversal, but support a zero-edge mass between edges (domains) with opposite mass signs. (d) To eliminate these zero-edge masses, the remaining spatial symmetries enforce their pairwise annihilation at symmetric edges (such as the edge located on the right side). (e) The trivial phase does not show any edge mass sign flip, and all boundaries are gapped out. (f) Hexagonal geometry with only zigzag edges in the HOTS or BOTS shows the same zero energy in-gap states localized at the corners (red spots).

a gap closing and reopening at one of the zigzag edges [right edge of Fig. 2(d2) and edge-2 in Fig. 2(d3)], which we call the BOTS phase transition. Note that the bulk remains gapped during this transition (black part of the energy spectrum in the third and fourth rows of Fig. 2).

### Symmetries

Equation (1) has particle-hole symmetry  $\Xi = \tau_x \mathcal{K}_{[k \rightarrow -k]}$  and time-reversal symmetry  $\Theta = s_y \tau_z \mathcal{K}_{[k \rightarrow -k]}$ , where  $\mathcal{K}$  is the complex-conjugate operator. The system is also invariant under a  $U(1)$  spin rotation, whose generator is given by  $S = s_z \tau_z$ . Moreover, Eq. (1) is invariant under a threefold rotational symmetry  $C_{3z} = e^{i\frac{\pi}{3} s_z \tau_z}_{[k \rightarrow \mathcal{R}_{2\pi/3} k]}$ , and mirror symmetry  $M_y = s_y [k_y \rightarrow -k_y]$ , where  $\mathcal{R}_\theta$  rotates momentum vector  $\mathbf{k}$  by  $\theta$  around the out-of-plane direction. Furthermore, when  $M = 0$ , Eq. (1) has inversion symmetry  $\mathcal{P} = \tau_z \sigma_x [k \rightarrow -k]$ , a sixfold rotational symmetry  $C_{6z} = e^{i\frac{\pi}{6} s_z \tau_z} \sigma_x \tau_z [k \rightarrow \mathcal{R}_{2\pi/6} k]$ , and a twofold rotational symmetry  $C_{2y} = s_y \sigma_x \tau_z [k_x \rightarrow -k_x]$ . When  $\mu = M = t_2 = 0$ , Eq. (1) additionally has a local symmetry  $\mathcal{L} = s_x \sigma_z \tau_y$  that commutes with  $S$ .

### First-order topological phase

As we have shown in Fig. 2(a), when  $\mu = M = t_2 = 0$ , the system supports gapless edge modes at all edges, implying the existence of a first-order topological phase. To see this, it is enough to rewrite  $H_{\text{BdG}}(\mathbf{k})$  using a unitary matrix  $U$  (given in Appendix A5) in the basis where both  $U^\dagger S U = s_z$  and  $U^\dagger \mathcal{L} U = \tau_z$  (and  $U^\dagger \sigma_z U = \sigma_z$ ) are diagonal and

$$t_1 H_1^{++}(\mathbf{k}) \sigma_x + t_1 H_1^{-+}(\mathbf{k}) \sigma_y + H_3^{+-}(k) \Delta_s \tau_z \sigma_z. \quad (2)$$

Therefore, in each sector of  $s_z = \pm 1$ ,  $H_{\text{BdG}}$  decomposes to two copies of the celebrated Haldane model [80] with opposite Chern numbers, similar to the two-dimensional quantum spin Hall insulator model proposed in graphene [81,82].

### Edge theory

Here, we derive an edge Hamiltonian at the boundary of a disk geometry to study the effect of nonzero  $\mu$ ,  $M$ , and  $t_2$  on the gapless boundary modes. The edge Hamiltonian of Eq. (2) composed of two counterpropagating chiral edge states can be written as

$$H_b(\theta, k_{\parallel}) = v_\theta \tau_z s_0 k_{\parallel}, \quad (3)$$

where  $v_\theta$  is the Fermi velocity of the gapless edge modes that depends on the polar angle  $\theta$ , and  $k_{\parallel}$  is the locally defined momentum tangent to the disk boundary [see Fig. 3(a)]. Note that the edge Hamiltonian has to satisfy all symmetries of Eq. (2), whose representations can be obtained by considering their definitions regarding the edge Hamiltonian and commutation or anticommutation relations between them (see Appendix B). The representations of particle-hole, time-reversal,  $\mathcal{L}$ , and  $\mathcal{S}$  symmetries are given by  $\Xi = s_x \tau_z \mathcal{K}_{[k_{\parallel} \rightarrow -k_{\parallel}]}$ ,  $\Theta = i s_y \tau_x \mathcal{K}_{[k_{\parallel} \rightarrow -k_{\parallel}]}$ ,  $\mathcal{L} = \tau_z$ , and  $\mathcal{S} = s_z$ , respectively. For spatial symmetries, we find that there are two types of symmetry operations: type-1 symmetries (proportional to  $\tau_y$  or  $\tau_z$ , such as  $C_{6z}$ ,  $C_{2y}$ , and  $\mathcal{P}$ ), and type-2 symmetries (proportional to  $\tau_x$  or  $\tau_0$ , such as  $C_{3z}$  and  $M_y$ ), where type-1 symmetries exchange the sublattice index, whereas type-2 symmetries preserve it.

### Possible edge mass

We can study the topological feature of this system by understanding how symmetry operations keep the edge Hamiltonian gapless [83]. The only edge mass that anticommutes with Eq. (3), and respects both  $\Xi$  and  $\Theta$ , is  $H_{\text{b.m.}}(\theta) = m(\theta) \tau_x$ . However, since  $\tau_x$  is odd under  $\mathcal{L}$ , the edge Hamiltonian remains gapless [ $m(\theta) = 0$ ] if  $\mathcal{L}$  is present (i.e.,  $\mu = M = t_2 = 0$ ). On the other hand, spatial symmetries relate edge masses at different  $\theta$ . If we add a mass term that respects certain symmetries to the bulk BdG Hamiltonian, we expect it to give an edge mass that also respects the same symmetries. The mass terms that are invariant under type-1 symmetries give  $m(\theta_p) = -m(\theta)$ , where  $\theta_p$  means the symmetric partner of  $\theta$  related by the given symmetry. Meanwhile, the mass terms that are invariant under type-2 symmetries give  $m(\theta_p) = +m(\theta)$ .

### HOTS

Let us first assume that the system is invariant under type-1 symmetries, which force mass sign changing for symmetry-related edges, giving zero-energy corner modes [84] [see Fig. 3(b)]. Then, the system belongs to HOTS [83,85]. We note that for the symmetric edges where  $\theta_p = \theta$ , such as  $\theta = \frac{\pi}{2}$  (armchair edges) under  $C_{2y}$ , the symmetry operation forces  $m(\theta_p \equiv \theta) = -m(\theta) = 0$ . Hence, the gapless boundary modes of the first-order topological phase are protected by symmetry operators on the symmetric edges. Accordingly, we can call this phase a  $C_{2y}$  protected topological crystalline superconductor [86]. Both  $\mu$  and  $t_2$  are invariant under type-1 symmetries and keep the gapless states of the armchair edges [Figs. 2(b2) and 2(b4)], while they gap out gapless states of zigzag edges [Figs. 2(b2) and 2(b3)]. Thus, the hexagonal



geometry with only zigzag edges hosts only corner modes [see Fig. 3(f)].

### BOTS

Now let us assume that the system is only invariant under type-2 symmetries, which do not force any topological gapless states, as symmetry-related edges obtain the same mass sign. Despite this fact, the system can still have two different phases that cannot be smoothly connected without a gap closing at a symmetric edge [see Figs. 3(c)–3(e)] [69,70]. For instance,  $\mu$  and  $M$  (and  $t_2$ ) are invariant under type-2 symmetries. Therefore, the HOTS (when  $\mu \neq 0$ ,  $M = 0$ ) can be smoothly transformed to BOTS by adding tiny  $|M|$ . Accordingly, although small  $M$  trivialize HOTS, still in-gap corner modes are protected because of the underlying BOTS phase [Figs. 2(c) or 3(f)]. These corner modes can be eliminated only by a BOTS phase transition through a gap closing at a symmetric edge [the zigzag edge located at the right side of Fig. 2(d)] when  $|M| \approx |\mu|$ .

### BOTS phase transition

We can obtain a rough estimation of the BOTS transition for geometries with only zigzag edges. For instance, consider the hexagonal geometry given in Fig. 3(f), where it has six edges that are labeled by  $ei$  ( $i = 1, \dots, 6$ ) and their corresponding edge masses are denoted by  $m_{ei}$ . We first obtain the edge mass at one of the edges (for instance  $e4$ ) and obtain others by symmetry considerations. To obtain  $m_{e4}$ , we need to find zero-energy modes at that edge (when  $\mu = t_2 = M = 0$ ) and then project  $\mu$ ,  $t_2$ , and  $M$  onto these zero-energy modes [87], which leads to  $m_{e4} = -\mu - 2t_2 + M$  (see Appendix C). The anticommutation of a mass term (i.e.,  $M$ ) with type-1 symmetries forces  $m(\theta_p) = m(\theta)$ . Thus, we obtain  $m_{e3} = \mu + 2t_2 + M$ , where signs of  $\mu$  and  $t_2$  are changed but  $M$  keeps its sign. Using type-2 symmetries, the  $e4$ ,  $e1$ , and  $e5$  ( $e2$ ,  $e3$ , and  $e6$ ) edges obtain the same edge mass. As a result, nearby edges of Fig. 3(f) obtain masses with opposite signs when  $|M| < |\mu + 2t_2|$  and give BOTS transition at  $|M| = |\mu + 2t_2|$ , which leads to a trivial phase by further increasing  $|M|$ .

### Large sublattice potential limit

In the large- $M$  limit, wave functions corresponding to the positive and negative energy bands of the honeycomb lattice are polarized on one sublattice [see Fig. 4(b)]. Therefore in this regime, the honeycomb lattice can be effectively decomposed into two triangular lattices, which we denote by  $\kappa = \pm 1$  [see Fig. 4(a)]. For instance, if we first take into account only  $t_1$  and  $M$ , we can write an effective Hamiltonian on the two triangular lattices with nearest-neighbor hopping  $t' = \frac{t_1^2}{2\kappa M}$  and on-site potential  $V' = \kappa M + \frac{zt_1^2}{2\kappa M}$  (see Appendix D). Here  $z$  is the coordination number of a site that counts the number of the honeycomb links connected to it. When  $|M| \gg |t_1|$ , we confirm that this effective Hamiltonian (by choosing  $z = 3$  for all sites) gives the identical bulk energy spectrum to the honeycomb lattice. However, the zigzag boundary modes [88,89] in the normal state of the honeycomb lattice are absent in

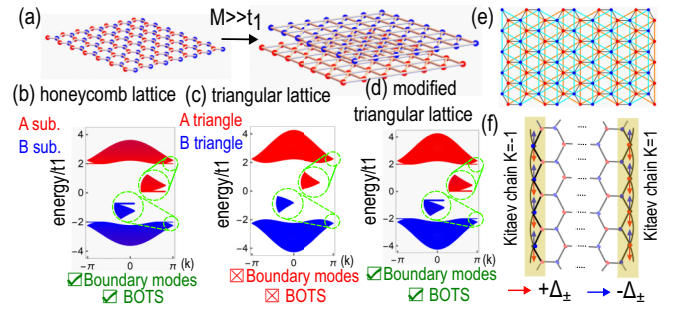


FIG. 4. (a) In the large sublattice potential  $M$  limit, the honeycomb lattice is effectively decomposed into two triangular lattices. (b) The normal state energy dispersion of the honeycomb lattice with strip geometry and zigzag edges, in which we only consider  $t_1$  and  $M$  ( $= 2t_1$ ). (c) The normal state energy dispersion of the effective triangular lattice (see the main text) with strip geometry and flat edges [see Fig. 4(e)]. (d) Same plot as (c) obtained after modifying the on-site potential on the boundary vertices. The green insets in (b)–(d) magnify energy dispersion around  $k = \pi$ . (e) Superimposed figure of the honeycomb lattice with two effective triangular lattices. (f) Effective Kitaev chains labeled by  $\kappa = \pm 1$  reside at the zigzag edges of the strip geometry of the honeycomb lattice.

the effective triangular lattices [compare Figs. 4(b) and 4(c)]. As we have shown in Fig. 4(d), we can restore the normal-state boundary modes in the triangular lattices by modifying the effective on-site potential considering the fact that at the zigzag boundary vertices,  $z = 2$  [see Fig. 4(e)]. Interestingly, turning on fSTP in the triangular lattice does not lead to any corner modes unless we modify the on-site potential at boundary vertices. Therefore, we can conclude that BOTS in the honeycomb lattice or the modified triangular lattice are related to the presence of these normal-state boundary modes.

### Effective Kitaev model and topological invariant

Because normal-state boundary modes are effectively localized at the boundary vertices [90], we can write an effective 1D Hamiltonian [91,92], in which the fSTP acts as a  $p$ -wave pairing for these vertices [see Fig. 4(f)]. Interestingly, this model can be considered as a generalization of the celebrated Kitaev model hosting Majorana end modes [77,93–95]. We can write a general effective Kitaev model including hopping, spin-orbit coupling (SOC),  $M$ , and pairing at the zigzag edges as

$$H_K(k) = H_N(k)\tau_z + H_{SO}(k)s_z + H_R(k)s_x + H_\Delta(k)s_x\tau_y, \quad (4)$$

where we apply Fourier transformation using  $k$ , the momentum parallel to the chain. In Eq. (4),  $H_N(k) = -\mu + \kappa M + 2t_2 \cos(k) + F^\kappa(k)$ ,  $H_{SO}(k) = 2\kappa\lambda_{SO} \sin(k)$ ,  $H_R(k) = 2\lambda_R \sin(k)$ ,  $H_\Delta(k) = 2\Delta_\kappa \sin(k)$ , and  $F^\kappa(k) = \sum_{n=0}^{n_c} t_n^\kappa \cos(nk)$ , where  $\lambda_{SO}$ ,  $\lambda_R$ , and  $t_n^\kappa$  are intrinsic SOC, Rashba SOC, and the effective hopping terms mediated by other (e.g., bulk) vertices, respectively. For instance, it is possible to write  $F^\kappa(k) \approx \frac{[1+\cos(k)]t_1^2}{\kappa M}$  by employing the effective Hamiltonian of the triangular lattice derived in the previous section as the simplest approximation. The topological state of Eq. (4) is protected by both particle-hole  $\Xi = \tau_x \mathcal{K}_{[k \rightarrow -k]}$  and time-reversal  $\Theta = s_y \tau_z \mathcal{K}_{[k \rightarrow -k]}$

symmetries (see also Appendixes E and I), where the system can have a nontrivial  $Z_2$  topological phase and the Majorana end modes come in pairs [94]. Note that when  $\lambda_R = \lambda_{SO} = 0$ , Eq. (4) is invariant under  $\tilde{\mathcal{M}}_y = \tau_z[k \rightarrow -k]$ , which acts effectively as an inversion symmetry for the Kitaev chain. Therefore, we can use the parity information  $\xi(k)$  at  $k = 0, \pi$  to obtain  $Z_2 = \prod'_{k=0,\pi} \xi(k)$  invariant, where the prime indicates that the multiplication is done for only one state of the Kramer's pair [94]. Because at  $k = 0, \pi$ , Eq. (4) reduces to  $H_N(k)\tau_z$ , we only need to check the sign changing between  $H_N(0)$  and  $H_N(\pi)$ . Therefore, we obtain  $Z_2 = \kappa \operatorname{sgn}(-\mu + \kappa M - 2t_2)$ , and the topological transition occurs at  $|M| = |\mu + 2t_2|$ , consistent with the edge state analysis. In the large- $M$  normal state of two Kitaev chains,  $\kappa = \pm 1$  are energetically separated, and accordingly for the geometry given in Fig. 4(f), only one of  $\kappa = \pm 1$  can be topological at most. Hence, we can interpret Fig. 2(c2) containing a Kitaev chain with a topologically nontrivial phase on the right zigzag edge. The introduction of SOC does not break the nontrivial  $Z_2$  topology of the effective Kitaev chain, as it preserves time-reversal symmetry. However, the presence of SOC can alter the equation defining the phase boundary, deviating slightly from  $|M| = |\mu + 2t_2|$ , due to the emergence of other effective terms (see Appendix G).

Note that in Eq. (4), considering sublattice-dependent pairings  $\Delta_{\kappa=\pm} = \Delta_{A,B}$  does not affect the topological properties of the effective Kitaev chains. Therefore, the presence of nonzero asymmetric fSTP  $\Delta_a = \frac{\Delta_A - \Delta_B}{2}$  in the honeycomb lattice, resulting from an imbalance between the local density of states in the  $A$  and  $B$  sublattices under a nonzero sublattice potential, cannot alter the phase transition. Furthermore, the dependence of the BOTS on the boundary modes in the normal states allows us to control the Majorana fermions using boundary engineering (see Appendix J). Additionally, a nontrivial topological state in the normal state always guarantees the existence of boundary modes, and it can lead to Majorana corner modes in the presence of fSTP (see Appendixes G and H for the quantum spin Hall effect and the quantum valley Hall effect [96], respectively).

#### IV. DISCUSSION

The stability of the BOTS we discussed can be understood by using the fact that the boundary Hamiltonian of the BOTS is equivalent to the Kitaev chain. According to the previous studies on the stability of the Kitaev chain against disorder and interaction, its topological property is stable against weak perturbation as long as the energy scale associated with the disorder or interaction is smaller than the energy gap of the Kitaev chain [97–103]. This indicates that the topological property of the BOTS is stable against weak perturbation.

We note that the BOTS is equivalent to a trivial superconductor under the periodic boundary condition. However, under the open boundary condition, it possesses two inequivalent phases: one is trivial and the other is topological, which cannot be continuously deformed to each other without a gap closing on its boundary. The underlying symmetry of BOTS forces the topological phase transition mediated by a gap closing on symmetric edges [70]. Moreover, the bulk in the BOTS

can provide enough carriers to derive the system toward fSTP instability.

Last but not least, although our discussion focused on the spin-full systems, the same idea can be applied to spin-polarized normal states such as gapped Dirac half-metals. By employing a similar analytic approach to the spin-polarized case, we found that the spin-polarized system also exhibits BOTS as in the case of spin-full systems (see, e.g., Appendix F).

#### V. CONCLUSION

In this work, we have studied the topological features of the  $f$ -wave superconductor in buckled honeycomb structures with sublattice potential. We first uncovered that despite breaking several symmetries by the sublattice potential, the remaining symmetries still protect BOTS with corner modes, and these corner modes disappear after a BOTS phase transition, mediated by gap closing on the symmetric edges. Furthermore, we uncover that generating boundary modes in the normal state (using boundary engineering or manipulating gate voltages) is an important step to realizing BOTS in the presence of fSTP. Our study can be extended to many recently discovered superconductors [1–4,104] in which superconductivity may obtain an fSTP symmetry [105,106].

#### ACKNOWLEDGMENTS

R.G. thanks Hongchul Choi for the discussions. R.G., S.H.L., and B.-J.Y. were supported by the Institute for Basic Science in Korea (Grant No. IBS-R009-D1), Samsung Science and Technology Foundation under Project No. SSTF-BA2002-06, and the National Research Foundation of Korea (NRF) grant funded by the Korea government (MSIT) (No. 2021R1A2C4002773 and No. NRF-2021R1A5A1032996).

#### APPENDIX A: THE DERIVATION OF THE BOGOLIUBOV–DE GENNES HAMILTONIAN

##### 1. Normal state

The general Hamiltonian of a honeycomb material with  $p_z$  orbital in the normal state reads

$$\begin{aligned}
 H = & -t_1 \sum_{\langle i,j \rangle, s} c_{is}^\dagger c_{js} + t_2 \sum_{\langle\langle i,j \rangle\rangle, s} c_{is}^\dagger c_{js} - \mu \sum_{i,s} c_{is}^\dagger c_{is} \\
 & + M \sum_{i,s} \kappa_i c_{is}^\dagger c_{is} + i\lambda_{SO} \sum_{\langle\langle i,j \rangle\rangle, ss'} v_{ij} c_{is}^\dagger [s_z]_{ss'} c_{js'} \\
 & + i\lambda_R \sum_{\langle\langle i,j \rangle\rangle, ss'} c_{is}^\dagger [(\vec{s} \times \hat{d}_{ij})_z]_{ss'} c_{js'}, \quad (\text{A1})
 \end{aligned}$$

where  $t_1$ ,  $t_2$ ,  $\mu$ ,  $\lambda_{SO}$ ,  $\lambda_R$ , and  $M$  are nearest-neighbor hopping, next-nearest-neighbor hopping, chemical potential, intrinsic spin-orbit coupling, Rashba spin-orbit coupling, and sublattice potential, respectively. In Eq. (A1),  $\langle i, j \rangle$  and  $\langle\langle i, j \rangle\rangle$  indicate nearest-neighbor and next-nearest-neighbor links in the honeycomb structure. The  $s_{\alpha=x,y,z}$  are usual Pauli matrices that act on the spin degree of freedom, and  $c_{is}^\dagger$ ,  $c_{is}$  are the creation and annihilation operator of an electron in the  $i$ th site with spin  $s = \uparrow, \downarrow$ , respectively. We set  $\kappa_{i \in A} = 1$  and  $\kappa_{i \in B} = -1$ , where  $A$  and  $B$  denote the two sublattices of the

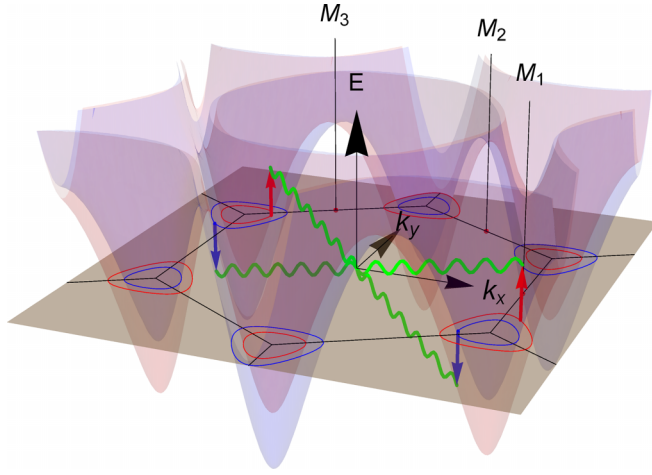


FIG. 5. Energy dispersion (normal state) of the honeycomb lattice for positive energy, when  $M \neq 0$  and  $\lambda_{SO} \neq 0$ . The intersection of energy dispersion (with some  $\mu$ ) is shown with blue and red contours, indicating their spin characteristic. The wiggly green lines show the instability toward non-FFLO superconductivity between opposite spins.

honeycomb lattice [Fig. 1(a)]. In Eq. (A1),  $\hat{d}_{ij}$  is the direction that connects  $i$  to  $j$  site and  $v_{ij} = \frac{\hat{d}_{ik} \times \hat{d}_{kj}}{|\hat{d}_{ik} \times \hat{d}_{kj}|}$ , where  $k$  is the intermediate site that connects  $i$  to site  $j$  by a nearest-neighbor path. By employing Fourier transformation  $c_{is}^\dagger = \frac{1}{\sqrt{N}} \sum_{\mathbf{k} \in \text{BZ}} e^{i\mathbf{k} \cdot \mathbf{r}_i} c_{\mathbf{k}i s}^\dagger$ ,  $c_{is} = \frac{1}{\sqrt{N}} \sum_{\mathbf{k} \in \text{BZ}} e^{-i\mathbf{k} \cdot \mathbf{r}_i} c_{\mathbf{k}i s}$ , we obtain

$$H = \sum_{\mathbf{k}} \sum_{\kappa\kappa'=\{A,B\}} \sum_{s,s'=\{\uparrow,\downarrow\}} c_{s\kappa\mathbf{k}}^\dagger [H_N(\mathbf{k})]_{s\kappa,s'\kappa'} c_{s'\kappa'\mathbf{k}}, \quad (\text{A2})$$

where  $\mathbf{k} = (k_x, k_y)$ , and

$$\begin{aligned} H_N(\mathbf{k}) = & t_1 H_1^{++}(\mathbf{k}) \sigma_x + t_1 H_{1'}^{+-}(\mathbf{k}) \sigma_y + t_2 H_2^{++}(\mathbf{k}) - \mu \\ & + \lambda_{SO} H_3^{+-}(\mathbf{k}) s_z \sigma_z + \lambda_R H_4^{+-}(\mathbf{k}) s_x \\ & + \lambda_R H_5^{+-}(\mathbf{k}) s_y + M \sigma_z. \end{aligned} \quad (\text{A3})$$

In Eq. (A3),  $\sigma_{\alpha=0,x,y,z}$  are the identity and Pauli matrices that act on the sublattice degree of freedom. Furthermore, we suppress the direct product notation  $\otimes$  between Pauli matrices and  $2 \times 2$  identity matrices, and we define  $H_1^{++}(\mathbf{k}) = -2 \cos \frac{k_x}{2} \cos \frac{\sqrt{3}k_y}{2} - \cos k_x$ ,  $H_{1'}^{+-}(\mathbf{k}) = 2 \sin \frac{k_x}{2} \cos \frac{k_x}{2} - 2 \sin \frac{k_x}{2} \cos \frac{\sqrt{3}k_y}{2}$ ,  $H_2^{++}(\mathbf{k}) = 4 \cos \frac{3k_x}{2} \cos \frac{\sqrt{3}k_y}{2} + 2 \cos \sqrt{3}k_y$ ,  $H_3^{+-}(\mathbf{k}) = 2 \sin \sqrt{3}k_y - 4 \cos \frac{3k_x}{2} \sin \frac{\sqrt{3}k_y}{2}$ ,  $H_4^{+-}(\mathbf{k}) = -2 \cos \frac{3k_x}{2} \sin \frac{\sqrt{3}k_y}{2} - 2 \sin \sqrt{3}k_y$ , and  $H_5^{+-}(\mathbf{k}) = 2\sqrt{3} \sin \frac{3k_x}{2} \cos \frac{\sqrt{3}k_y}{2}$ , respectively.

## 2. Pairing potential

The energy dispersion of Eq. (A3) in the presence of both  $\mu$  and  $\lambda_{SO}$  but without  $\lambda_R = 0$  is shown in Fig. 5. As we can see, the system has two valleys, and the Fermi contours along them are spin-polarized, and its polarization flips in different valleys. Considering the Fermi-contour geometry (red and blue contours in Fig. 5), and in the absence of Fulde-Ferrell-Larkin-Ovchinnikov (FFLO) superconductivity, the pairing

can occur among electrons with opposite spin and momenta, which can lead to both singlet and triplet pairing instabilities. Furthermore, in the buckled honeycomb structure, such as silicene, we can tune both  $\mu$  and  $M$  using a double-gate setup [see Fig. 1(b)], which may enhance or change superconductivity instability. Indeed, it is shown that the triplet  $f$ -wave pairing can be dominated over a singlet  $d$ -wave channel in the presence of large  $M$  by polarizing wave function in one of the sublattices [55] [see Fig. 1(c)]. The  $f$ -wave pairing has a  $\sin 3\theta_{ij}$  characteristic, where  $\theta_{ij}$  is the azimuthal angle from the horizontal direction. Therefore, the pairing potential between the nearest-neighbor vertices is zero, while for the next-nearest neighbors, the sign of pairing flips six times by rotating around a given site [see Fig. 1(a)]. In the main text, we assume that  $\lambda_R, \lambda_{SO} \ll M$ , which can be satisfied for a low buckled honeycomb structure under a strong electric field, and we expect  $f$ -wave pairing can be dominated even in the presence of small spin-orbit coupling. Because of  $M \neq 0$ , the  $f$ -wave pairing potential  $\Delta_A, \Delta_B$  can be different for  $A$  and  $B$  sublattices, respectively. The  $f$ -wave pairing in real space can be modeled by

$$H_{sc} = \sum_{\langle(i,j)\rangle} \sum_{ss'} v_{ij} (\kappa_i \Delta_s + \Delta_a) c_{is}^\dagger [s_x]_{ss'} c_{is'}^\dagger, \quad (\text{A4})$$

where we define a symmetric  $\Delta_s = (\Delta_A + \Delta_B)/2$  and an asymmetric  $\Delta_a = (\Delta_A - \Delta_B)/2$  pairing potential. Note that  $v_{ij} = \kappa_i \sin 3\theta_{ij}$ . We can multiply Eq. (A4) by any arbitrary phase factor, which, although it may change the form of the Hamiltonian and symmetries representation, does not have any physical importance.

## 3. BdG Hamiltonian

By obtaining Fourier transformation of Eq. (A4),  $H_{sc} = -i \sum_{\mathbf{k}} c_{s\kappa\mathbf{k}}^\dagger H_3^{+-}(\mathbf{k}) (k) [(\Delta_s + \sigma_z \Delta_a) s_x]_{s\alpha,s'\alpha'} c_{s'\kappa\mathbf{k}}^\dagger$ . We can write the Bogoliubov-de Gennes (BdG) Hamiltonian as

$$H_{\text{BdG}} = \sum_{\mathbf{k}} a_{s\kappa\tau\mathbf{k}}^\dagger [H_{\text{BdG}}(\mathbf{k})]_{s\kappa\tau,s'\kappa'\tau'} a_{s'\kappa'\tau'\mathbf{k}}, \quad (\text{A5})$$

where  $\tau = \pm 1$  indicate electron and hole in the Nambu space;  $a_{s\kappa(+1)\mathbf{k}}^\dagger = c_{s\kappa\mathbf{k}}^\dagger$ ,  $a_{s\kappa(-1)\mathbf{k}}^\dagger = c_{s\kappa-\mathbf{k}}$ ,  $a_{s\kappa(+1)\mathbf{k}} = c_{s\kappa\mathbf{k}}$ ,  $a_{s\kappa(-1)\mathbf{k}} = c_{s\kappa-\mathbf{k}}^\dagger$ , and we assume summation over repeated indices. The  $H_{\text{BdG}}(\mathbf{k})$  is given as follows:

$$\begin{aligned} H_{\text{BdG}}(\mathbf{k}) = & t_1 H_1^{++}(\mathbf{k}) \sigma_x \tau_z + t_1 H_{1'}^{+-}(\mathbf{k}) \sigma_y \tau_z + t_2 H_2^{++}(\mathbf{k}) \tau_z \\ & + \lambda_{SO} H_3^{+-}(\mathbf{k}) s_z \sigma_z + \lambda_R H_4^{+-}(\mathbf{k}) s_x \\ & + \lambda_R H_5^{+-}(\mathbf{k}) s_y \tau_z \\ & - \mu \tau_z + M \sigma_z \tau_z + H_3^{+-}(\mathbf{k}) (\Delta_s + \sigma_z \Delta_a) s_x \tau_y, \end{aligned} \quad (\text{A6})$$

where  $\tau_{0,x,y,z}$  are identity and Pauli matrices that act on the electron-hole degrees of freedom.

## 4. Symmetries

In this section, we present the extended symmetries of (A6). For simplicity, let us first assume that the honeycomb lattice is unbuckled. Equation (A6) generally (in the existence of all terms) has particle-hole symmetry  $\Xi = \tau_x \mathcal{K} [\mathbf{k} \rightarrow -\mathbf{k}]$ , time-reversal symmetry  $\Theta = s_y \tau_z \mathcal{K}$

TABLE I. Symmetry operators [in the bulk representation Eq. (A8) and edge representation Eq. (B1)] and their algebra, where their commutation or anticommutation  $XX' - sX'X = 0$  are shown with  $s = \pm 1$ , respectively. For the cases in which they do not either commute or anticommute, we leave their blocks empty. The last two columns show the algebra between symmetry operators (edge representation) and  $\tau_z, \tau_x$ .

X	Bulk representation		Algebra between symmetry operators: $XX' - sX'X = 0$												Edge representation		Algebra			
	Operation	$\mathbf{k} \rightarrow$	$X^2$	$\Xi$	$\Theta$	$\mathcal{L}$	$\mathcal{S}$	$\mathcal{M}_y$	$\mathcal{C}_{2x}$	$\mathcal{P}$	$\mathcal{M}_x$	$\mathcal{C}_{2z}$	$\mathcal{C}_{2y}$	$\mathcal{C}_{3z}$	$\mathcal{C}_{6z}$	Operation	$\theta \rightarrow$	$k_{\parallel} \rightarrow$	$\tau_z$	$\tau_x$
$\Xi$	$is_x\tau_z\sigma_z\mathcal{K}$	$-\mathbf{k}$	+1	+1	+1	+1	-1	-1	-1	-1	+1	+1	+1	+1	-1	$s_x\tau_z\mathcal{K}$	$\theta$	$-k_{\parallel}$	+1	-1
$\Theta$	$s_y\tau_x\mathcal{K}$	$-\mathbf{k}$	-1	+1	+1	-1	-1	-1	-1	+1	-1	-1	-1	+1	+1	$is_y\tau_x\mathcal{K}$	$\theta$	$-k_{\parallel}$	-1	+1
$\mathcal{L}$	$\tau_z$	$\mathbf{k}$	+1	+1	-1	+1	+1	-1	-1	+1	-1	+1	-1	+1	+1	$\tau_z$	$\theta$	$k_{\parallel}$	+1	-1
$\mathcal{S}$	$s_z$	$\mathbf{k}$	+1	-1	-1	+1	+1	-1	-1	+1	-1	+1	-1	+1	+1	$s_z$	$\theta$	$k_{\parallel}$	+1	+1
$\mathcal{M}_y$	$s_y\tau_x$	$(k_x, -k_y)$	+1	-1	-1	-1	-1	+1	-1	+1	-1	+1	$\dots$	$\dots$	$s_y\tau_x$	$-\theta$	$-k_{\parallel}$	-1	+1	
$\mathcal{C}_{2x}$	$s_x\tau_x$	$(k_x, -k_y)$	+1	-1	-1	-1	-1	-1	+1	+1	+1	-1	-1	$\dots$	$\dots$	$s_x\tau_x$	$-\theta$	$-k_{\parallel}$	-1	+1
$\mathcal{P}$	$\sigma_x$	$-\mathbf{k}$	+1	-1	+1	+1	+1	+1	+1	+1	+1	+1	+1	+1	+1	$s_z\tau_z$	$\theta + \pi$	$k_{\parallel}$	+1	-1
$\mathcal{M}_x$	$s_x\tau_x\sigma_x$	$(-k_x, k_y)$	+1	+1	-1	-1	-1	-1	+1	+1	+1	-1	-1	$\dots$	$\dots$	$s_y\tau_y$	$\pi - \theta$	$-k_{\parallel}$	-1	-1
$\mathcal{C}_{2z}$	$s_z\sigma_x$	$-\mathbf{k}$	+1	+1	-1	+1	+1	-1	-1	+1	-1	+1	-1	+1	+1	$\tau_z$	$\theta + \pi$	$k_{\parallel}$	+1	-1
$\mathcal{C}_{2y}$	$s_y\tau_x\sigma_x$	$(-k_x, k_y)$	+1	+1	-1	-1	-1	+1	-1	+1	-1	+1	$\dots$	$\dots$	$s_x\tau_y$	$\pi - \theta$	$-k_{\parallel}$	-1	-1	
$\mathcal{C}_{3z}$	$\frac{1+i\sqrt{3}s_z}{2}$	$\mathcal{R}_{2\pi/3}\mathbf{k}$	$-\mathcal{C}_{3z}^{-1}$	+1	+1	+1	+1	$\dots$	$\dots$	+1	$\dots$	+1	$\dots$	+1	+1	$\frac{1+i\sqrt{3}s_z}{2}$	$\theta + 2\pi/3$	$k_{\parallel}$	+1	+1
$\mathcal{C}_{6z}$	$\frac{\sqrt{3}\sigma_x + is_z\tau_x}{2}$	$\mathcal{R}_{2\pi/6}\mathbf{k}$	$\mathcal{C}_{3z}$	-1	+1	+1	+1	$\dots$	$\dots$	+1	$\dots$	+1	$\dots$	+1	+1	$\frac{\sqrt{3}s_z\tau_z + i\tau_x}{2}$	$\theta + 2\pi/6$	$k_{\parallel}$	+1	-1

$[\mathbf{k} \rightarrow -\mathbf{k}]$ , and chiral symmetry  $\Pi = s_y\tau_y$ , where  $\mathcal{K}$  is the complex-conjugate operator.

Moreover, Eq. (A6) is invariant under a threefold rotational symmetry  $\mathcal{C}_{3z} = e^{i\frac{\pi}{3}s_z\tau_z}[\mathbf{k} \rightarrow \mathcal{R}_{2\pi/3}\mathbf{k}]$ , mirror symmetry  $\mathcal{M}_y = s_y[(k_x, k_y) \rightarrow (k_x, -k_y)]$ , and a twofold rotational symmetry  $\mathcal{C}_{2x} = s_x\tau_x[(k_x, k_y) \rightarrow (k_x, -k_y)]$  ( $\lambda_R = 0$ ), in addition to  $U(1)$  spin rotation around the out-of-plane direction, whose generator is given by  $\mathcal{S} = s_z\tau_z$  ( $\lambda_R = 0$ ).

Furthermore, when  $\Delta_a = M = 0$ , Eq. (A6) has inversion symmetry  $\mathcal{P} = \tau_z\sigma_x[\mathbf{k} \rightarrow -\mathbf{k}]$  ( $\lambda_R = 0$ ), a mirror symmetry  $\mathcal{M}_x = s_x\sigma_x[(k_x, k_y) \rightarrow (-k_x, k_y)]$ , and a sixfold rotational symmetry  $\mathcal{C}_{6z} = e^{i\frac{\pi}{6}s_z\tau_z}\sigma_x\tau_z[\mathbf{k} \rightarrow \mathcal{R}_{2\pi/6}\mathbf{k}]$  and two twofold rotation symmetries  $\mathcal{C}_{2z} = s_z\sigma_x[\mathbf{k} \rightarrow -\mathbf{k}]$  and  $\mathcal{C}_{2y} = s_y\sigma_x\tau_z[(k_x, k_y) \rightarrow (-k_x, k_y)]$  ( $\lambda_R = 0$ ).

When  $\mu = M = t_2 = 0$ , Eq. (A6) has an additional local symmetry  $\mathcal{L} = s_x\sigma_z\tau_y$  ( $\lambda_{s_0} = 0$ ) that commutes with  $\mathcal{S}$ .

On the other hand, when  $\Delta_a = \Delta_s = 0$ , Eq. (A6) has two additional symmetries regarding  $U(1)$  gauge symmetry  $\mathcal{T} = \tau_z$  and spin rotational symmetry  $\tilde{\mathcal{S}} = s_z$  ( $\lambda_R = 0$ ), where  $\mathcal{S} = \tilde{\mathcal{S}}\mathcal{T}$ .

Note that considering the buckling property, some symmetry operators such as  $\mathcal{M}_x$  and  $\mathcal{C}_{2x}$  are not true spatial symmetry of the system. However, they are related to the other true spatial symmetry of the system by multiplication of  $\mathcal{S}$ , for instance  $\mathcal{M}_x = -i\mathcal{C}_{2y}\mathcal{S}$  and  $\mathcal{C}_{2x} = i\mathcal{M}_y\mathcal{S}$ , respectively.

### 5. Basis transformation

In studying the first-order topological phase and deriving the edge Hamiltonian, we rewrite Eq. (A6) in a basis in which  $\mathcal{L}$ ,  $\mathcal{S}$ , and  $\sigma_z$  are diagonal. We use

$$U = e^{i\pi s_x\sigma_z\left(-\frac{1}{4} + \frac{1}{3\sqrt{3}}\tau_x + \frac{1}{3\sqrt{3}}\tau_z\right) + i\pi\frac{1}{3\sqrt{3}}\tau_y} \quad (\text{A7})$$

and get ( $\lambda_{s_0} = \lambda_R = \Delta_a = 0$ )

$$U^\dagger H_{\text{BdG}}(\mathbf{k})U = t_1 H_1^{++}(\mathbf{k})\sigma_x + t_1 H_1^{-+}(\mathbf{k})\sigma_y + \tau_z H_3^{+-}(k)\Delta_s\sigma_z + [t_2 H_2^{++}(k) - \mu]\tau_x + M\sigma_z\tau_x. \quad (\text{A8})$$

### APPENDIX B: EDGE HAMILTONIAN AND SYMMETRY REPRESENTATION

In the main text, we argue that due to the chiral propagating of the edge modes in opposite directions, the edge Hamiltonian is given by

$$H_{\text{edge}}(\theta, k_{\parallel}) = v_{\theta}\tau_z s_0 k_{\parallel}. \quad (\text{B1})$$

We can justify this edge Hamiltonian as follows. First  $s_z$  is absent from Eq. (A8). Thus, the edge Hamiltonian is independent of  $s_z$ . Second, we knew that in Eq. (A8) if we change the sign of  $\Delta_s$  (when  $\mu = M = 0$ ) the propagation of chiral modes flips and therefore the edge Hamiltonian has to be proportional to  $\tau_z$ .

In the following, we obtain a representation of the symmetry operators for the edge Hamiltonian. To derive a representation of symmetry operators, we first note that  $\mathcal{L}^{\text{edge}} = \tau_z$  and  $\mathcal{S}^{\text{edge}} = s_z$ . Next, we determine the particle-hole operator, regarding the edge Hamiltonian (anticommuting with the Hamiltonian and flipping the sign of  $k_{\parallel}$ ), and its relation with  $\mathcal{L}^{\text{edge}}$  and  $\mathcal{S}^{\text{edge}}$  (given in Table I). However, the edge Hamiltonian and  $\mathcal{L}^{\text{edge}}$  and  $\mathcal{S}^{\text{edge}}$  are invariant under  $\exp(i\phi + i\alpha\tau_z + i\beta s_z + i\gamma\tau_z s_z)$ . Therefore, we have the freedom to choose the particle-hole symmetry representation. After fixing the particle-hole symmetry representation, we can uniquely determine a representation for time-reversal symmetry by considering its definition regarding the edge Hamiltonian (commuting with the Hamiltonian and flipping the sign of  $k_{\parallel}$ ), and its relation with  $\mathcal{S}^{\text{edge}}$ ,  $\mathcal{L}^{\text{edge}}$ , and  $\Xi^{\text{edge}}$ . We choose  $\Xi^{\text{edge}} = s_x\tau_z\mathcal{K}[k_{\parallel} \rightarrow -k_{\parallel}]$ , and we obtain  $\Theta^{\text{edge}} = is_y\tau_x\mathcal{K}[k_{\parallel} \rightarrow -k_{\parallel}]$ .

Next, we determine the representation of other spatial symmetries. Generally, all of the spatial symmetry operators have to commute with the edge Hamiltonian. To obtain them, we should know how reflection, rotations, and inversion transform  $k_{\parallel}$ . In Table I we show the effect of symmetry operators on  $k_{\parallel}$ , which can be easily found by considering Fig. 3(a) of the main text [we illustrate rotation and reflection symmetries



in Fig. 3(a)]. If a given symmetry operator flips (keeps) the sign of  $k_{\parallel}$ , it has to anticommute (commute) with  $\tau_z$  (we have tabulated them in Table I). To continue, we need to find the algebra or relation among different symmetry operators from their bulk definition (given in Table I) and then construct the edge representation for them by considering the same algebra. We start with  $\mathcal{M}_y^{\text{edge}}$ . Considering the definition of  $\mathcal{M}_y^{\text{edge}}$  regarding the edge Hamiltonian and its relations with  $\mathcal{S}^{\text{edge}}$ ,  $\mathcal{L}^{\text{edge}}$ ,  $\mathcal{X}^{\text{edge}}$ , and  $\mathcal{Y}^{\text{edge}}$ , we obtain an arbitrary combination of two options. This is because  $H_{\text{edge}}$ ,  $\mathcal{L}^{\text{edge}}$ ,  $\mathcal{S}^{\text{edge}}$ ,  $\mathcal{X}^{\text{edge}}$ , and  $\mathcal{Y}^{\text{edge}}$  are still invariant under  $\exp(i\beta s_z)$ . We choose  $\mathcal{M}_y^{\text{edge}} = s_y \tau_x [k_{\parallel} \rightarrow -k_{\parallel}]$ , and the representation of other symmetry operators can be determined uniquely by doing the same procedure (all given in Table I).

As we have discussed in the main text, the only edge mass that respects both particle-hole and time-reversal operators is  $m(\theta)\tau_x$ . If we assume that in the bulk an  $\mathcal{L}$ -symmetry-breaking term commutes with certain symmetry operations, then similarly its corresponding mass  $m(\theta)\tau_x$  has to commute with the edge representation of those symmetry operators. Therefore, if that symmetry operator anticommutes (commutes) with  $\tau_x$ , then  $m(\theta)$  should flip (keeps) its sign on the symmetric partner  $m(\theta_{\text{sp}}) = -m(\theta)$  [ $m(\theta_{\text{sp}}) = m(\theta)$ ]. We also tabulate the commutation or anticommutation of the edge representation of symmetry operators with  $\tau_x$  in Table I.

Furthermore, under time-reversal and particle-hole symmetry, we can also add the term  $m'\tau_z s_z$  to the edge Hamiltonian Eq. (B1). Considering Eq. (B1) and the edge mass and  $m'\tau_z s_z$ , we can write

$$H'_{\text{edge}}(\theta, k_{\parallel}) = v_{\theta} \tau_z s_0 k_{\parallel} + m \tau_x + m' \tau_z s_z. \quad (\text{B2})$$

The energy spectrum of Eq. (B2) is given by

$$E(k) = \pm \sqrt{(k \pm m')^2 + m^2}. \quad (\text{B3})$$

The topological phase transition occurs when  $k = \pm m'$  and  $m = 0$ . Nonzero values of  $m'$  alter the BOTS transition in momentum space. It is noteworthy that, in the presence of  $\lambda_{\text{SO}}$ , the BOTS transition does not occur at the time-reversal invariant point (i.e.,  $k = 0$  in our low-energy Dirac theory), as demonstrated in Appendix G. This observation suggests that spin-orbit coupling introduces additional terms in the effective edge Hamiltonian.

### APPENDIX C: EDGE THEORY

We can find the zero-energy modes of Eq. (A8) by expanding the Hamiltonian up to the linear order of  $k_x$  around  $M_1$  [87]. To describe the zero-energy edge modes, we substitute  $k_x \rightarrow -i\partial_x$ , where  $x = 0$  is the position of the edge that separates the interior region  $x < 0$  from its exterior  $x > 0$ , achieving

$$\left( -t_1 \zeta(x) \frac{\sigma_x + \sqrt{3}\sigma_y}{2} - i\partial_x (\sqrt{3}\sigma_x - \sigma_y) t_1 \right) \psi_{s_z = \pm 1, \tau_z = \pm 1}(x) = 0, \quad (\text{C1})$$

where we introduce  $\zeta(x) = -\text{sgn}(x)$ ,  $|x| \gg 0$ . The following wave functions satisfy this equation:

$$\psi_{s_z = \pm 1, \tau_z = \pm 1}(x) = \frac{1}{\mathcal{N}} e^{\frac{1}{2} \int \zeta(x) dx} |s_z = \pm 1, \tau_z = \pm 1, \sigma_z = 1\rangle, \quad (\text{C2})$$

where  $\mathcal{N}$  is the normalization factor. By projecting  $\mu$ ,  $M$ , and  $t_2$  onto  $\psi_{s_z = \pm 1, \tau_z = \pm 1}(x)$  subspace, we obtain  $m_{e4} \equiv m(\theta = 0) = -\mu - 2t_2 + M$ .

### APPENDIX D: LARGE SUBLATTICE POTENTIAL LIMIT: EFFECTIVE HAMILTONIAN

In the large sublattice potential limit, we can decompose the Hamiltonian of the honeycomb lattice into two triangular lattices. For simplicity, consider the Hamiltonian of a honeycomb lattice (normal state) with sublattice potential and nearest-neighbor hopping terms,

$$t_{ij} \psi_j^A - M \psi_i^B = E \psi_i^B, \quad (\text{D1})$$

$$t_{ij} \psi_j^B + M \psi_i^A = E \psi_i^A, \quad (\text{D2})$$

where  $\psi_i^A$  and  $\psi_i^B$  are the wave function at site  $i$  and sublattices  $A$  and  $B$ , respectively. We want to rewrite Eqs. (D1) and (D2) in such a way that  $A$  and  $B$  sublattice sectors are decomposed. To do this, we can rewrite Eqs. (D1) and (D2) as

$$\psi_i^B = \frac{1}{E + M} t_{ij} \psi_j^A, \quad (\text{D3})$$

$$\psi_i^A = \frac{1}{E - M} t_{ij} \psi_j^B, \quad (\text{D4})$$

which lead to

$$t_{ij} \frac{1}{E - M} t_{jk} \psi_k^B - M \psi_i^B = E \psi_i^B, \quad (\text{D5})$$

$$t_{ij} \frac{1}{E + M} t_{jk} \psi_k^A + M \psi_i^A = E \psi_i^A. \quad (\text{D6})$$

In the large sublattice limit, we can approximate  $E = \mp M$  in the denominator of Eqs. (D5) and (D6), respectively,

$$t_{ij} \frac{1}{-2M} t_{jk} \psi_k^B - M \psi_i^B = E \psi_i^B, \quad (\text{D7})$$

$$t_{ij} \frac{1}{+2M} t_{jk} \psi_k^A + M \psi_i^A = E \psi_i^A. \quad (\text{D8})$$

These Hamiltonians describe two triangular lattices with effective on-site and nearest-neighbor hopping. We can read the effective hopping ( $k \neq i$ ) and on-site potential ( $k = i$ ) as  $t^2/(\kappa 2M)$  and  $z t^2/(\kappa 2M) + \kappa M$ , respectively, where  $z$  is the coordination number.

### APPENDIX E: WINDING NUMBER AS A TOPOLOGICAL INVARIANT FOR THE EFFECTIVE KITAEV CHAIN

The topological phase of the effective Kitaev chain also protected by the chiral symmetry when  $\lambda_R = 0$ . To see this, we rewrite the effective Kitaev Hamiltonian in the basis where both chiral symmetry  $\Pi = s_y \tau_y$  and  $S = s_z \tau_z$  are diagonal ( $|\Pi = 1, S = 1\rangle$ ,  $|\Pi = 1, S = -1\rangle$ ,  $|\Pi = -1, S = 1\rangle$ ,  $|\Pi = -1, S = -1\rangle$ ), getting a block off-diagonalized matrix

$$U^\dagger H_{\text{Kitaev}}(k) U = \begin{pmatrix} 0 & h(k) \\ h^\dagger(k) & 0 \end{pmatrix}, \quad (\text{E1})$$



where  $U$  is a unitary matrix and

$$h(k) = \begin{pmatrix} -H_N(k) - H_{SO}(k) + iH_\Delta(k) & H_R(k) \\ H_R(k) & -H_N(k) + H_{SO}(k) - iH_\Delta(k) \end{pmatrix}. \quad (\text{E2})$$

When  $\lambda_R = 0$ , the topological invariant of the effective Kitaev chains is given by the winding number of each diagonal element of  $h(k)$ , or equivalently  $\nu_{S=\pm 1} = \frac{1}{2\pi} \int dk h_{SS}^{-1}(k) \partial_k h_{SS}(k)$ . In the topological phase, the two winding numbers are nonzero but have opposite signs  $\nu_1 = -\nu_2 = \pm 1$ . After turning on  $\lambda_R \neq 0$ , we have to calculate the total winding number of the whole  $h(k)$  or equivalently  $\nu_t = \frac{1}{2\pi} \int dk \text{tr}(h^{-1}(k) \partial_k h(k))$ , which already gives zero for  $\lambda_R = 0$ . Therefore, in the presence of  $\lambda_R$ , the winding number cannot diagnose the topological phase.

#### APPENDIX F: SPIN-POLARIZED CASE

In the Dirac half-metal material, one spin component is gapped out, and the remaining Dirac cones are gapless and spin-polarized. Introducing the sublattice potential gapped out the remaining Dirac cone. Alternatively, we can also generalize this material to gapped Dirac half-metal material, where Dirac cones in both spin sectors are gapped out with a spin-dependent sublattice potential  $M_s \sigma_z$ , but the sublattice potential for one spin sector is bigger than the other, for instance  $M_\uparrow \gg M_\downarrow$ . Therefore, the Fermi contours are polarized in one spin sector, and triplet pairing is the only possible pairing instability. As we have discussed before, the existence of normal states (edge modes in the absence of superconductivity) is the key to realizing the BOTS (when superconductivity is turned on), and we can write down an effective Hamiltonian for the spin-polarized Kitaev chain

$$H_{\text{SPKC}}(k) = H_N(k) \tau_z + H_{SO}(k) \tau_0 + H_\Delta(k) \tau_y. \quad (\text{F1})$$

In Eq. (F1),  $H_N(k) = -\mu + \kappa M_\downarrow + 2t_2 \cos(k) + F_{\text{boundary}}^\kappa(k)$ ,  $H_{SO}(k) = 2\kappa \lambda_{SO} \sin(k)$ ,  $H_R(k) = 2\lambda_R \sin(k)$ ,  $H_\Delta(k) = 2\Delta_\kappa \sin(k)$ , and  $F_{\text{boundary}}^\kappa(k) = \sum_{n=0}^{n_c} t_n^\kappa \cos(nk)$ , where  $t_n^\kappa$  are the effective hopping terms mediated by other (e.g., bulk) vertices. The particle-hole and time-reversal symmetry are given by  $\Xi = \tau_x \mathcal{K}[k \rightarrow -k]$  and  $\Theta = \mathcal{K}[k \rightarrow -k]$ , respectively. In the absence of spin-orbit coupling, Eq. (F1) is invariant under a chiral symmetry  $\tau_x$  and  $\mathcal{C}_{2x} = \tau_z[k \rightarrow -k]$  symmetry. The chiral symmetry allows us to define the winding number, and similar to the spin-full calculation, it gives the nontrivial topological phase if  $|M| < |\mu + 2t|$ . On the other hand,  $Z_2$  topological invariant can be determined by parity information on  $k = 0, \pi$ , which gives similar results to the winding number calculation. In the presence of SOC, we cannot use the winding number, but the  $Z_2$  topological invariant is well-defined and cannot be changed until the edge Hamiltonian goes to gap-closing.

#### APPENDIX G: $f$ -WAVE SPIN-TRIPLET PAIRING AND QUANTUM SPIN HALL EFFECT, LARGE SPIN-ORBIT COUPLING LIMIT

In the large  $\lambda_{SO} > M$  limit, the normal state of the system has a nontrivial topological phase, which is known as the

quantum spin Hall effect [81]. In the following, we derive the edge Hamiltonian using symmetry analysis. When ( $\mu = t_2 = M = \lambda_R = \Delta_s = \Delta_a = 0$ ), Eq. (A6) is reduced to

$$H_{\text{BdG}}(\mathbf{k}) = t_1 H_1^{++}(\mathbf{k}) \sigma_x \tau_z + t_1 H_1^{-+}(\mathbf{k}) \sigma_y \tau_z + \lambda_{SO} H_3^{+-}(\mathbf{k}) s_z \sigma_z. \quad (\text{G1})$$

This Hamiltonian is invariant under  $\Xi$ ,  $\Theta$ ,  $\mathcal{C}_{6z}$ ,  $\mathcal{C}_{2z}$ ,  $\mathcal{C}_{2y}$ ,  $\mathcal{M}_x$ ,  $\mathcal{P}$ ,  $\mathcal{C}_{3z}$ ,  $\mathcal{C}_{2x}$ ,  $\mathcal{M}_y$ ,  $\mathcal{S}$ ,  $\mathcal{T}$ , and  $\tilde{\mathcal{S}}$ . In this Appendix, for simplicity, we assume  $\lambda_R = 0$ .

It is helpful to rewrite Eq. (G1) in a new basis using a unitary transformation

$$U = \exp \frac{1}{4} i\pi(\sigma_z - \sigma_x \tau_z), \quad (\text{G2})$$

which leads to

$$U^\dagger H_{\text{BdG}}(\mathbf{k}) U = t_1 H_1^{++}(\mathbf{k}) \sigma_x + t_1 H_1^{-+}(\mathbf{k}) \sigma_y + \lambda_{SO} H_3^{+-}(k) \sigma_z s_z. \quad (\text{G3})$$

Equation (G3) describes two copies ( $\tau_z = \pm 1$ ) of the celebrated Kane-Mele model, and it hosts two chiral boundary modes propagating in opposite directions. Therefore, the edge Hamiltonian can be described by

$$H_{\text{edge}}^0(\theta, k_\parallel) = v_\theta k_\parallel s_z \tau_0. \quad (\text{G4})$$

We obtain the symmetries representation of Eq. (G4) using the same procedure that we used in Appendix B, where we tabulated them in Table II.

In the following, we try to find a general edge Hamiltonian regarding nonzero  $\Delta_s$ ,  $\mu$ ,  $M$ , and  $\Delta_a$ . Each of these terms has a certain commutation or anticommutation relation with symmetry operators, and we assume that their main effect also respects those relations in the edges Hamiltonian.

The  $\mu$ ,  $t_2$ , and  $M$  respect all of the local symmetries ( $\Xi$ ,  $\Theta$ ,  $\mathcal{T}$ ,  $\tilde{\mathcal{S}}$ , and  $\mathcal{S}$ ). The only  $k_\parallel$ -independent term that can satisfy these symmetries is

$$W_\alpha(\theta) \tau_z, \quad (\text{G5})$$

where  $\alpha = \mu, t_2, M$ . These terms are symmetric under  $\mathcal{M}_y$ ,  $\mathcal{C}_{2x}$ , and  $\mathcal{C}_{3z}$ . Accordingly, and using Table II,  $W_\alpha(\theta) = W_\alpha(-\theta) = W_\alpha(\theta + 2\pi/3)$ . However, although  $\mu$  and  $t_2$  are symmetric under  $\mathcal{M}_x$ ,  $\mathcal{C}_{2y}$ ,  $\mathcal{P}$ ,  $\mathcal{C}_{2z}$ , and  $\mathcal{C}_{6z}$  (commuting with them),  $M$  is not (anticommuting with them). Thus,  $\mu$  and  $t_2$  lead to (where  $\alpha = \mu, t_2$ )

$$W_\alpha(\theta) = W_\alpha(\pi - \theta) = W_\alpha(\pi + \theta) = W_\alpha(\theta + 2\pi/6), \quad (\text{G6})$$

while  $M$  leads to

$$\begin{aligned} W_M(\theta) &= -W_M(\pi - \theta) \\ &= -W_M(\pi + \theta) \\ &= -W_M(\theta + 2\pi/6). \end{aligned} \quad (\text{G7})$$

This means that in the  $\mathcal{M}_x$  symmetric edges (armchair edges),  $W_M(\theta) = 0$ . Note that  $W_{\mu, t_2, M}(\theta) \tau_z$  does not commute with

TABLE II. Symmetry operators [in the bulk representation Eq. (G3) and edge representation Eq. (G4)] and their algebra, where their commutation or anticommutation  $XX' - sX'X = 0$  are shown with  $s = \pm 1$ , respectively. For the cases in which they do not either commute or anticommute, we leave their blocks empty. The last two columns show the algebra between symmetry operators (edge representation) and  $s_z, s_x \tau_x$ .

X	Bulk representation		Algebra between symmetry operators: $XX' - sX'X = 0$												Edge representation		Algebra			
	Operation	$\mathbf{k} \rightarrow$	$X^2$	$\Xi$	$\Theta$	$\mathcal{T}$	$\tilde{\mathcal{S}}$	$\mathcal{M}_y$	$\mathcal{C}_{2x}$	$\mathcal{P}$	$\mathcal{M}_x$	$\mathcal{C}_{2z}$	$\mathcal{C}_{2y}$	$\mathcal{C}_{3z}$	$\mathcal{C}_{6z}$	Operation	$\theta \rightarrow$	$k_{\parallel} \rightarrow$	$s_z$	$s_x \tau_x$
$\Xi$	$-i\tau_x \sigma_z \mathcal{K}$	$-\mathbf{k}$	+1	+1	+1	-1	+1	-1	-1	-1	+1	+1	+1	+1	-1	$\tau_x \mathcal{K}$	$\theta$	$-k_{\parallel}$	+1	+1
$\Theta$	$s_y \mathcal{K}$	$-\mathbf{k}$	-1	+1	+1	+1	-1	-1	-1	+1	-1	-1	+1	+1	+1	$is_y \mathcal{K}$	$\theta$	$-k_{\parallel}$	-1	-1
$\mathcal{T}$	$\tau_z$	$\mathbf{k}$	+1	-1	+1	+1	+1	+1	+1	+1	+1	+1	+1	+1	+1	$\tau_z$	$\theta$	$k_{\parallel}$	+1	-1
$\tilde{\mathcal{S}}$	$s_z$	$\mathbf{k}$	+1	+1	-1	+1	+1	-1	-1	+1	-1	+1	+1	+1	+1	$s_z$	$\theta$	$k_{\parallel}$	+1	-1
$\mathcal{M}_y$	$s_y$	$(k_x, -k_y)$	+1	-1	-1	+1	-1	+1	-1	+1	-1	+1	...	...	...	$s_y$	$-\theta$	$-k_{\parallel}$	-1	-1
$\mathcal{C}_{2x}$	$s_x \tau_z$	$(k_x, -k_y)$	+1	-1	-1	+1	-1	-1	+1	+1	+1	-1	-1	...	...	$s_x \tau_z$	$-\theta$	$-k_{\parallel}$	-1	+1
$\mathcal{P}$	$\sigma_x$	$-\mathbf{k}$	+1	-1	+1	+1	+1	+1	+1	+1	+1	+1	+1	+1	+1	$\tau_z$	$\theta + \pi$	$k_{\parallel}$	+1	-1
$\mathcal{M}_x$	$s_x \tau_z \sigma_x$	$(-k_x, k_y)$	+1	+1	-1	+1	-1	-1	+1	+1	+1	-1	-1	...	...	$s_x$	$\pi - \theta$	$-k_{\parallel}$	-1	+1
$\mathcal{C}_{2z}$	$s_z \tau_z \sigma_x$	$-\mathbf{k}$	+1	+1	-1	+1	+1	-1	-1	+1	-1	+1	+1	+1	+1	$s_z$	$\theta + \pi$	$k_{\parallel}$	+1	-1
$\mathcal{C}_{2y}$	$s_y \sigma_x$	$(-k_x, k_y)$	+1	+1	-1	+1	-1	+1	-1	+1	-1	+1	...	...	...	$s_y \tau_z$	$\pi - \theta$	$-k_{\parallel}$	-1	+1
$\mathcal{C}_{3z}$	$\frac{1+i\sqrt{3}s_z \tau_z}{2}$	$\mathcal{R}_{2\pi/3} \mathbf{k}$	$-\mathcal{C}_{3z}^{-1}$	+1	+1	+1	+1	...	...	+1	...	+1	...	+1	+1	$\frac{1+i\sqrt{3}s_z \tau_z}{2}$	$\theta + 2\pi/3$	$k_{\parallel}$	+1	+1
$\mathcal{C}_{6z}$	$\frac{\sqrt{3}\sigma_x + is_z \sigma_x \tau_z}{2}$	$\mathcal{R}_{2\pi/6} \mathbf{k}$	$\mathcal{C}_{3z}$	-1	+1	+1	+1	...	...	+1	...	+1	...	+1	+1	$\frac{\sqrt{3}\tau_z + is_z}{2}$	$\theta + 2\pi/6$	$k_{\parallel}$	+1	-1

the Hamiltonian, and it cannot gap out the edge Hamiltonian [see Figs. 6(a1) and 6(b1)].

As we discussed before, nonzero  $\Delta_s \neq 0$  (or  $\Delta_a \neq 0$ ) breaks  $\mathcal{T}$  and  $\tilde{\mathcal{S}}$ , but the system is still invariant under  $\mathcal{S}$ . If we assume three remaining local symmetries  $\Xi$ ,  $\Theta$ , and  $\mathcal{S}$ , we can add the following terms to the edge Hamiltonian, which break  $\tilde{\mathcal{S}}$  and  $\mathcal{T}$ :

$$\delta_{\alpha}(\theta) s_y \tau_y + \Delta_{\alpha}^{\text{edge}}(\theta) k_{\parallel} s_x \tau_x, \quad \alpha = \Delta_s, \Delta_a. \quad (\text{G8})$$

These terms anticommute with Eq. (G4) and can gap it out [Fig. 6(a2)]. Note that even with nonzero  $\Delta_s$  or  $\Delta_a$ , the system is invariant under  $\mathcal{M}_y$ ,  $\mathcal{C}_{2x}$ , and  $\mathcal{C}_{3z}$ . Using Table II, we obtain

$$\delta_{\alpha}(\theta) = \delta_{\alpha}(-\theta) = \delta_{\alpha}(\theta + 2\pi/3) \quad (\text{G9})$$

and

$$\Delta_{\alpha}^{\text{edge}}(\theta) = \Delta_{\alpha}^{\text{edge}}(-\theta) = \Delta_{\alpha}^{\text{edge}}(\theta + 2\pi/3). \quad (\text{G10})$$

Although  $\Delta_s$  is symmetric under  $\mathcal{M}_x$ ,  $\mathcal{C}_{2y}$ ,  $\mathcal{P}$ ,  $\mathcal{C}_{2z}$ , and  $\mathcal{C}_{6z}$  (commuting with them),  $\Delta_a$  are not (anticommuting with them). Using Table II, we obtain

$$\delta_{\Delta_s}(\theta) = -\delta_{\Delta_s}(\pi + \theta) = -\delta_{\Delta_s}(\pi - \theta), \quad (\text{G11})$$

$$\Delta_{\Delta_s}^{\text{edge}}(\theta) = -\Delta_{\Delta_s}^{\text{edge}}(\pi + \theta) = -\Delta_{\Delta_s}^{\text{edge}}(\pi - \theta), \quad (\text{G12})$$

$$\delta_{\Delta_a}(\theta) = \delta_{\Delta_a}(\pi + \theta) = \delta_{\Delta_a}(\pi - \theta), \quad (\text{G13})$$

and

$$\Delta_{\Delta_a}^{\text{edge}}(\theta) = \Delta_{\Delta_a}^{\text{edge}}(\pi + \theta) = \Delta_{\Delta_a}^{\text{edge}}(\pi - \theta). \quad (\text{G14})$$

This means that at the  $\mathcal{M}_x$  symmetric edges (armchair edges),  $\delta_{\Delta_s}(\theta) = \Delta_{\Delta_s}^{\text{edge}}(\theta) = 0$ .

We can write the general edge Hamiltonian as follows:

$$H_{\text{edge}}(\theta, k_{\parallel}) = v_{\theta} k_{\parallel} s_z + W(\theta) \tau_z + \delta(\theta) s_y \tau_y + \Delta^{\text{edge}}(\theta) k_{\parallel} s_x \tau_x, \quad (\text{G15})$$

where

$$W(\theta) = W_{\mu}(\theta) + W_{t_2}(\theta) + W_M(\theta) + W_{\text{other corrections}}(\theta), \quad (\text{G16})$$

$$\delta(\theta) = \delta_{\Delta_s}(\theta) + \delta_{\Delta_a}(\theta) + \delta_{\text{other corrections}}(\theta), \quad (\text{G17})$$

$$\Delta^{\text{edge}}(\theta) = \Delta_{\Delta_s}^{\text{edge}}(\theta) + \Delta_{\Delta_a}^{\text{edge}}(\theta) + \Delta_{\text{other corrections}}^{\text{edge}}(\theta). \quad (\text{G18})$$

As we have discussed before,  $\mathcal{M}_y$ ,  $\mathcal{C}_{2x}$ , and  $\mathcal{C}_{3z}$  give

$$W(\theta) = W(-\theta) = W(\theta + 2\pi/3), \quad (\text{G19})$$

$$\delta(\theta) = \delta(-\theta) = \delta(\theta + 2\pi/3), \quad (\text{G20})$$

$$\Delta^{\text{edge}}(\theta) = \Delta^{\text{edge}}(-\theta) = \Delta^{\text{edge}}(\theta + 2\pi/3). \quad (\text{G21})$$

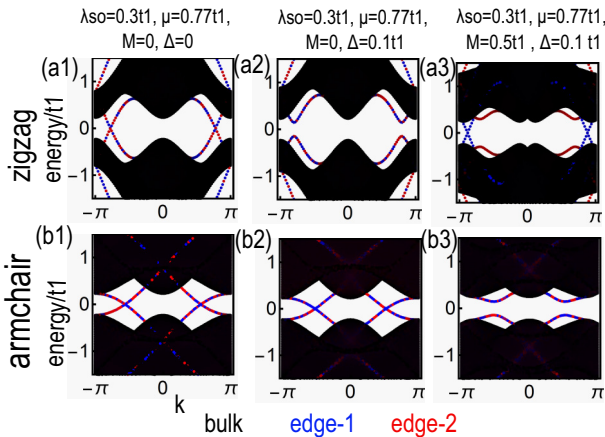


FIG. 6. Energy dispersion (superconducting states or BdG Hamiltonian) of a strip geometry of the honeycomb lattice with  $f$ -wave spin-triplet pairing and spin-orbit coupling.

However, when  $M = \Delta_a = 0$ , then  $\mathcal{M}_x$ ,  $\mathcal{C}_{2y}$ ,  $\mathcal{C}_{2z}$ ,  $\mathcal{P}$ , and  $\mathcal{C}_{6z}$  give

$$W(\theta) = W(\pi - \theta) = W(\pi + \theta) = W(\theta + 2\pi/6), \quad (\text{G22})$$

$$\delta(\theta) = -\delta(\pi - \theta) = -\delta(\pi + \theta) = -\delta(\theta + 2\pi/6), \quad (\text{G23})$$

$$\begin{aligned} \Delta^{\text{edge}}(\theta) &= -\Delta^{\text{edge}}(\pi - \theta) = -\Delta^{\text{edge}}(\pi + \theta) \\ &= -\Delta^{\text{edge}}\left(\theta + \frac{2\pi}{6}\right). \end{aligned} \quad (\text{G24})$$

In the following, we discuss different topological phases of the system by studying the gapless state of the general edge Hamiltonian Eq. (G15) that is forced by symmetries relations. We first discuss the case of  $\mu = t_2 = M = \Delta_a = 0$ , and then we discuss possible topological phases.

When  $\mu = t_2 = M = 0$  (but nonzero  $\Delta_s$  and  $\Delta_a$ ), the bulk Hamiltonian is invariant under two other local symmetries  $O_1 = \tau_x \sigma_z s_z$  and  $O_2 = \tau_y \sigma_z$  [in the representation of Eq. (A6)]. We obtain their edge Hamiltonian representation as  $O_1^{\text{edge}} = \tau_x$  and  $O_2^{\text{edge}} = s_z \tau_y$  by using their relationships (commutation or anticommutation) with other local symmetries  $\Xi$ ,  $\Theta$ , etc. Note that  $O_1^{\text{edge}}$  and  $O_2^{\text{edge}}$  force  $W(\theta) = \delta(\theta) = 0$  in Eq. (G15). Consequently, Eq. (G15) remains gapless, the  $f$ -wave pairing potential cannot gap out the normal state, and the system can be considered as a first-order topological phase, which indicates that gapless states exist along all boundaries. This phase is connected ( $\Delta_a = 0$ ,  $\lambda_R \rightarrow 0$ ) to the first-order topological state that we discuss in the main text.

If we turn on  $\mu \neq 0$  or  $t_2 \neq 0$ , but keep  $M = \Delta_a = 0$ , a nonzero  $W(\theta)$ ,  $\delta(\theta)$ , and  $\Delta^{\text{edge}}(\theta)$  can be induced in the edge Hamiltonian. However, symmetry constraints (type-1 symmetry group) force sign changing for  $\Delta^{\text{edge}}(\theta_{\text{sp}}) = -\Delta(\theta)$  and  $\delta(\theta_{\text{sp}}) = -\delta^{\text{edge}}(\theta)$ , which means that they vanish at the symmetric edges (armchair edges). Therefore, the normal modes remain gapless, and  $f$ -wave spin-triplet pairing does not gap them out in the  $\mathcal{M}_x$  symmetric edges [compare Figs. 6(a2) and 6(b2)]. We can call this system a crystalline topological superconductor. Furthermore, due to the sign changing of  $\delta(\theta)$  and  $\Delta^{\text{edge}}(\theta)$ , this system becomes a HOTS in the absence of symmetric edges [39].

By introducing  $M \neq 0$  or  $\Delta_a \neq 0$ , type-1 symmetries will be broken, and there is no constraint that forces gapless states for Eq. (G15). Therefore, the system is no longer HOTS, and crystalline topological superconductivity breaks down. Consequently, gapless edge modes along  $\mathcal{M}_x$  symmetric edges are gapped out [see Fig. 6(b3)]. However, the system can still obtain a nontrivial BOTS phase, where the topological phase transitions from the nontrivial phase to the trivial phase mediated by a gap closing at an  $\mathcal{M}_y$  symmetric edge. The energy spectrum of Eq. (G15) is zero (gapless) if  $W(\theta) = -v(\theta) \frac{\delta(\theta)}{\Delta^{\text{edge}}(\theta)}$  and  $k_{\parallel} = \frac{\delta(\theta)}{\Delta^{\text{edge}}(\theta)}$ . Now consider two  $\mathcal{M}_y$  symmetric edges that are located at  $\theta = 0, \pi$ . Doing the same procedure that we used in Appendix C, we can find  $W(0) \approx -(\mu + 2t_2) + M$ , while  $W(\pi) \approx -(\mu + 2t_2) - M$ . Therefore, in the absence of  $\delta(0, \pi) = 0$ , the BOTS phase transition is given by  $|M| = |\mu + 2t_2|$ , which is the same as that obtained in other limits. This BOTS phase transition is not dependent on spin-orbit coupling strength, so reducing  $\lambda_{\text{so}}$  does not change it. Finally, a trivial insulator is

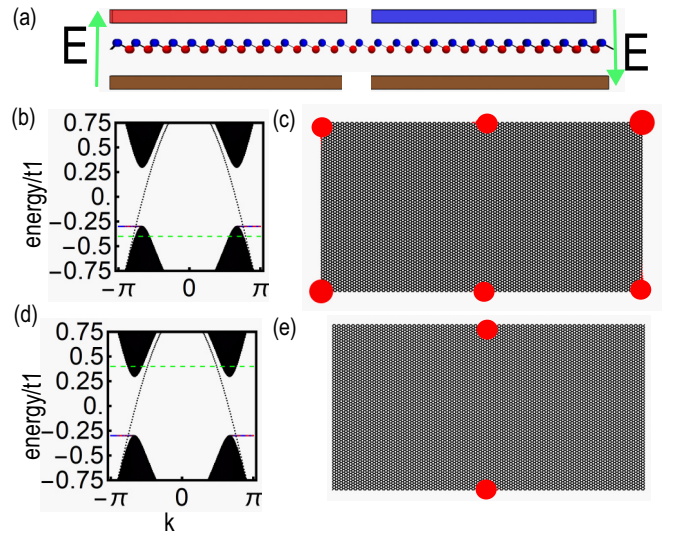


FIG. 7. The  $f$ -wave spin-triplet pairing and valley quantum Hall effect. (a) The double gate setup with an opposite electric field on the opposite halves of the system. (b), (d) The energy dispersion (normal state) of a zigzag strip geometry with an opposite sublattice mass  $|M| = 0.3t_1$  ( $t_1 = 1$ ) on the two sides of the system. (c), (e) Majorana zero-energy modes (red spots), when we turn on  $f$ -wave spin-triplet pairing  $\Delta_s = 0.1t_1$ . We set (c)  $\mu = -0.4$ , (e)  $\mu = 0.4$ , which is shown by green dashed lines in (b) and (d), respectively. The number of Majorana zero modes in (c) and (e) amounts to 12 and 4, respectively.

derived from the topological quantum spin Hall phase by reducing  $\lambda_{\text{so}}$ . Though in this process the normal state undergoes a bulk gap closing, in the superconducting phase this process is always gapped. This phase is thus connected to the large sublattice potential limit that we discussed in the main text.

In Fig. 6(a3) we plot the BOTS phase transition, which appears for  $k \neq 0, \pi$  (corresponding to  $k = 0$  in our low-energy Dirac theory), and it indicates nonzero  $\delta(\theta)$ . Note that  $\delta(\theta)$  breaks  $\mathcal{T}$  symmetry and is a superconducting pairing potential. Because  $\delta(\theta)_{s_y \tau_y}$  is  $k_{\parallel}$ -independent, we can interpret it as an effective spin-singlet pairing potential. We confirm that in the absence of  $\lambda_{\text{so}}$  the BOTS transition happens in  $k = 0$ , indicating  $\delta(\theta)$  is emerging from a combination of spin-orbit coupling,  $f$ -wave spin-triplet pairing, and sublattice potential processes.

#### APPENDIX H: $f$ -WAVE SPIN-TRIPLET PAIRING AND VALLEY QUANTUM HALL EFFECT

Boundary modes in the honeycomb structures can be achieved by applying the opposite sublattice potential on the two sides of the system. This can be done by applying an opposite electric field on two opposite sides of a buckled honeycomb lattice [Fig. 7(a)], in which a boundary mode appears in the middle of them [Fig. 7(b)]. Actually, this boundary mode is related to the edge mode of a topological phase with a nonzero valley Chern number (equal to 1), called the valley quantum Hall effect, and it is protected by the absence of scattering between two valleys [96]. One can imagine this boundary mode as a 1D chain that lives in the middle of the

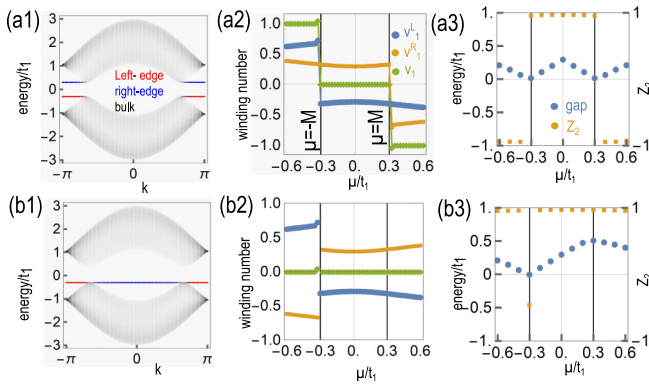


FIG. 8. The BOTS transition in a strip geometry where (a) two edges are zigzag, and (b) one is zigzag and the other is dangling. We plot energy dispersion (normal state), the edge-resolved winding number, and the  $Z_2$  topological invariant in the left, center, and right panels. In this calculation, we set  $M = 0.3t_1$ ,  $\Delta_s = 0.1t_1$ , and other parameters to zero. We also show the energy gap (in the superconducting state) in the right panels.

system. We show in Figs. 7(c) and 7(e) that the Majorana zero-energy modes appear (when  $\Delta_s \neq 0$ ) at the ends of this effective 1D (Kitaev) chain. The corner modes in Fig. 7(c) are related to the normal modes that appear at the zigzag edges (two effective Kitaev chains that live on the two sides of the system). These normal modes obtain the same energy due to opposite sublattice potential on the two sides of the system [see the degenerate blue and red edge states of the energy spectrum in Fig. 7(b)].

### APPENDIX I: TOPOLOGICAL INVARIANT FOR THE STRIP OF THE HONEYCOMB LATTICE

We can generalize the  $Z_2$  topological invariant or winding number to calculate the topological states of the strip

geometry. To confirm the Kitaev chain picture, we define edge-resolved winding-number  $\nu_{S=\pm 1} = \nu_S^L + \nu_S^R$ , where  $\nu_S^{L,R} = \frac{1}{2\pi} \int dk \text{Tr}^{L,R}(\tilde{h}_S^{-1}(k) \partial_k \tilde{h}_S(k))$ , and  $\tilde{h}_S$  is the off-diagonal part of the BdG Hamiltonian in the basis of chiral symmetry and  $\mathcal{S}$ . The  $\text{Tr}^{L,R}$  is the partial trace that only sums over indices that belong to the left ( $L$ ) or right ( $R$ ) part of the system [two opposite halves of the strip geometry; see Fig. 1(a)] [72]. Note that although  $\nu_S$  is a quantized number,  $\nu_S^{R,L}$  are not. However, the jumping of  $\nu_S^{L,R}$  across the topological phase transition is a good signature for the topological phase transition [72]. Furthermore, we numerically calculate the  $Z_2$  topological invariant for the strip geometry (see Ref. [94] for the procedure). In Figs. 8(a1)–8(a3) we compare the  $Z_2$ , winding number, and energy gap for a system with zigzag edges, which confirms the applicability of these topological invariants for diagnosing topological phases.

### APPENDIX J: BOTS AT THE DANGLING EDGE

The fact that the existence of a nontrivial topological phase with corner modes depends on the normal-state condition leads us to design different edge terminations and therefore manipulate corner modes. For instance, suppose in designing strip geometry that we instead terminate two edges with the same sublattice atoms [for instance, remove the red vertices on the right side of Fig. 1(a)]. In this case, one edge is zigzag and the other is dangling. The coordination number on the dangling edge is  $z = 1$ , and we expect normal modes for them. However, its energy is the same as the zigzag normal modes [compare Figs. 8(a1) and 8(b1)]. Therefore, the two edges obtain the same topological state simultaneously, where the jump of the edge-resolved winding number shows a topological phase transition for both edges [see Fig. 8(b2)]. Note that  $Z_2$  and  $\nu_S$  cannot diagnose this topological phase transition [see Fig. 8(b3)].

- [1] T. T. Heikkilä, Surprising superconductivity of graphene, *Science* **375**, 719 (2022).
- [2] H. Zhou, T. Xie, T. Taniguchi, K. Watanabe, and A. F. Young, Superconductivity in rhombohedral trilayer graphene, *Nature (London)* **598**, 434 (2021).
- [3] H. Zhou, L. Holleis, Y. Saito, L. Cohen, W. Huynh, C. L. Patterson, F. Yang, T. Taniguchi, K. Watanabe, and A. F. Young, Isospin magnetism and spin-polarized superconductivity in bernal bilayer graphene, *Science* **375**, 774 (2022).
- [4] Y. Cao, V. Fatemi, S. Fang, K. Watanabe, T. Taniguchi, E. Kaxiras, and P. Jarillo-Herrero, Unconventional superconductivity in magic-angle graphene superlattices, *Nature (London)* **556**, 43 (2018).
- [5] S.-L. Yang, J. A. Sobota, C. A. Howard, C. J. Pickard, M. Hashimoto, D. H. Lu, S.-K. Mo, P. S. Kirchmann, and Z.-X. Shen, Superconducting graphene sheets in  $\text{CaC}_6$  enabled by phonon-mediated interband interactions, *Nat. Commun.* **5**, 3493 (2014).
- [6] K. Kanetani, K. Sugawara, T. Sato, R. Shimizu, K. Iwaya, T. Hitosugi, and T. Takahashi, Ca intercalated bilayer graphene

as a thinnest limit of superconducting  $\text{C}_6\text{Ca}$ , *Proc. Natl. Acad. Sci. USA* **109**, 19610 (2012).

- [7] S. Ichinokura, K. Sugawara, A. Takayama, T. Takahashi, and S. Hasegawa, Superconducting calcium-intercalated bilayer graphene, *ACS Nano* **10**, 2761 (2016).
- [8] B. M. Ludbrook, G. Levy, P. Nigge, M. Zonno, M. Schneider, D. J. Dvorak, C. N. Veenstra, S. Zhdanovich, D. Wong, P. Dosanjh, C. Straßer, A. Stöhr, S. Forti, C. R. Ast, U. Starke, and A. Damascelli, Evidence for superconductivity in Li-decorated monolayer graphene, *Proc. Natl. Acad. Sci. USA* **112**, 11795 (2015).
- [9] H. Toyama, R. Akiyama, S. Ichinokura, M. Hashizume, T. Iimori, Y. Endo, R. Hobara, T. Matsui, K. Horii, S. Sato, T. Hirahara, F. Komori, and S. Hasegawa, Two-dimensional superconductivity of Ca-intercalated graphene on SiC: Vital role of the interface between monolayer graphene and the substrate, *ACS Nano* **16**, 3582 (2022).
- [10] Y. Fukaya, K. Yada, A. Hattori, and Y. Tanaka, Pairing mechanism of unconventional superconductivity in doped kane–mele model, *J. Phys. Soc. Jpn.* **85**, 104704 (2016).



- [11] S. Wolf, T. Gardener, K. Le Hur, and S. Rachel, Topological superconductivity on the honeycomb lattice: Effect of normal state topology, *Phys. Rev. B* **105**, L100505 (2022).
- [12] K. Lee, T. Hazra, M. Randeria, and N. Trivedi, Topological superconductivity in Dirac honeycomb systems, *Phys. Rev. B* **99**, 184514 (2019).
- [13] M. Ezawa, Exact solutions for two-dimensional topological superconductors: Hubbard interaction induced spontaneous symmetry breaking, *Phys. Rev. B* **97**, 241113(R) (2018).
- [14] B. Roy and I. F. Herbut, Unconventional superconductivity on honeycomb lattice: Theory of kekule order parameter, *Phys. Rev. B* **82**, 035429 (2010).
- [15] J.-H. Zhou, T. Qin, and J.-R. Shi, Intra-valley spin-triplet  $p + ip$  superconducting pairing in lightly doped graphene, *Chin. Phys. Lett.* **30**, 017401 (2013).
- [16] A. M. Black-Schaffer and C. Honerkamp, Chiral  $d$ -wave superconductivity in doped graphene, *J. Phys.: Condens. Matter* **26**, 423201 (2014).
- [17] A. M. Black-Schaffer and S. Doniach, Resonating valence bonds and mean-field  $d$ -wave superconductivity in graphite, *Phys. Rev. B* **75**, 134512 (2007).
- [18] A. M. Black-Schaffer, W. Wu, and K. Le Hur, Chiral  $d$ -wave superconductivity on the honeycomb lattice close to the mott state, *Phys. Rev. B* **90**, 054521 (2014).
- [19] B. Uchoa and A. H. Castro Neto, Superconducting States of Pure and Doped Graphene, *Phys. Rev. Lett.* **98**, 146801 (2007).
- [20] J. P. L. Faye, P. Sahebsara, and D. Sénéchal, Chiral triplet superconductivity on the graphene lattice, *Phys. Rev. B* **92**, 085121 (2015).
- [21] J. L. McChesney, A. Bostwick, T. Ohta, T. Seyller, K. Horn, J. González, and E. Rotenberg, Extended van Hove Singularity and Superconducting Instability in Doped Graphene, *Phys. Rev. Lett.* **104**, 136803 (2010).
- [22] S.-J. O, Y.-H. Kim, O.-G. Pak, K.-H. Jong, C.-W. Ri, and H.-C. Pak, Competing electronic orders on a heavily doped honeycomb lattice with enhanced exchange coupling, *Phys. Rev. B* **103**, 235150 (2021).
- [23] X. Wu, M. Fink, W. Hanke, R. Thomale, and D. Di Sante, Unconventional superconductivity in a doped quantum spin hall insulator, *Phys. Rev. B* **100**, 041117(R) (2019).
- [24] W.-C. Lee, C. Wu, and S. Das Sarma,  $f$ -wave pairing of cold atoms in optical lattices, *Phys. Rev. A* **82**, 053611 (2010).
- [25] L.-Y. Xiao, S.-L. Yu, W. Wang, Z.-J. Yao, and J.-X. Li, Possible singlet and triplet superconductivity on honeycomb lattice, *Europhys. Lett.* **115**, 27008 (2016).
- [26] V. Crépel, T. Cea, L. Fu, and F. Guinea, Unconventional superconductivity due to interband polarization, *Phys. Rev. B* **105**, 094506 (2022).
- [27] S. Wolf, D. Di Sante, T. Schwemmer, R. Thomale, and S. Rachel, Triplet Superconductivity from Nonlocal Coulomb Repulsion in an Atomic Sn Layer Deposited onto a Si(111) Substrate, *Phys. Rev. Lett.* **128**, 167002 (2022).
- [28] M. Biderang, M.-H. Zare, and J. Sirker, Topological superconductivity in Sn/Si(111) driven by nonlocal coulomb interactions, *Phys. Rev. B* **106**, 054514 (2022).
- [29] C. Honerkamp, Density Waves and Cooper Pairing on the Honeycomb Lattice, *Phys. Rev. Lett.* **100**, 146404 (2008).
- [30] M. L. Kiesel, C. Platt, W. Hanke, D. A. Abanin, and R. Thomale, Competing many-body instabilities and unconventional superconductivity in graphene, *Phys. Rev. B* **86**, 020507(R) (2012).
- [31] M. Y. Kagan, V. A. Mitskan, and M. M. Korovushkin, Effect of the long-range coulomb interaction on the phase diagram of the kohn-luttinger superconducting state in idealized graphene, *J. Low Temp. Phys.* **185**, 508 (2016).
- [32] M. Y. Kagan, V. Mitskan, and M. Korovushkin, Kohn-luttinger superconductivity in monolayer and bilayer semimetals with the dirac spectrum, *J. Exp. Theor. Phys.* **119**, 1140 (2014).
- [33] R. Nandkishore, R. Thomale, and A. V. Chubukov, Superconductivity from weak repulsion in hexagonal lattice systems, *Phys. Rev. B* **89**, 144501 (2014).
- [34] Y.-Z. Chou, F. Wu, J. D. Sau, and S. Das Sarma, Acoustic-phonon-mediated superconductivity in moiréless graphene multilayers, *Phys. Rev. B* **106**, 024507 (2022).
- [35] Y.-Z. Chou, F. Wu, J. D. Sau, and S. Das Sarma, Correlation-Induced Triplet Pairing Superconductivity in Graphene-Based Moiré Systems, *Phys. Rev. Lett.* **127**, 217001 (2021).
- [36] Y. He, K. Yang, J. B. Hauck, E. J. Bergholtz, and D. M. Kennes, Superconductivity of repulsive spinless fermions with sublattice potentials, *Phys. Rev. Res.* **5**, L012009 (2023)
- [37] H. Sainz-Cruz, P. A. Pantaleón, V. T. Phong, A. Jimeno-Pozo, and F. Guinea, Junctions and superconducting symmetry in twisted bilayer graphene, [arXiv:2211.11389](https://arxiv.org/abs/2211.11389).
- [38] T. Li, M. Geier, J. Ingham, and H. D. Scammell, Higher-order topological superconductivity from repulsive interactions in kagome and honeycomb systems, *2D Mater.* **9**, 015031 (2022).
- [39] H. D. Scammell, J. Ingham, M. Geier, and T. Li, Intrinsic first- and higher-order topological superconductivity in a doped topological insulator, *Phys. Rev. B* **105**, 195149 (2022).
- [40] Y. Wang, Y. Ke, Y.-J. Chang, Y.-H. Lu, J. Gao, C. Lee, and X.-M. Jin, Constructing higher-order topological states in higher dimensions, *Phys. Rev. B* **104**, 224303 (2021).
- [41] L. Trifunovic and P. W. Brouwer, Higher-order topological band structures, *Phys. Status Solidi B* **258**, 2000090 (2021).
- [42] F. Schindler, A. M. Cook, M. G. Vergniory, Z. Wang, S. S. P. Parkin, B. A. Bernevig, and T. Neupert, Higher-order topological insulators, *Sci. Adv.* **4**, eaat0346 (2018).
- [43] T. Neupert and F. Schindler, Topological crystalline insulators, in *Topological Matter: Lectures from the Topological Matter School 2017*, edited by D. Bercioux, J. Cayssol, M. G. Vergniory, and M. Reyes Calvo (Springer International, Cham, 2018), pp. 31–61.
- [44] Z. Yan, Higher-Order Topological Odd-Parity Superconductors, *Phys. Rev. Lett.* **123**, 177001 (2019).
- [45] D. Vu, R.-X. Zhang, and S. Das Sarma, Time-reversal-invariant  $C_2$ -symmetric higher-order topological superconductors, *Phys. Rev. Res.* **2**, 043223 (2020).
- [46] M. Kheirkhah, Z. Yan, Y. Nagai, and F. Marsiglio, First- and Second-Order Topological Superconductivity and Temperature-Driven Topological Phase Transitions in the Extended Hubbard Model with Spin-Orbit Coupling, *Phys. Rev. Lett.* **125**, 017001 (2020).
- [47] J. Ahn and B.-J. Yang, Higher-order topological superconductivity of spin-polarized fermions, *Phys. Rev. Res.* **2**, 012060(R) (2020).
- [48] Y. Wang, M. Lin, and T. L. Hughes, Weak-pairing higher order topological superconductors, *Phys. Rev. B* **98**, 165144 (2018).

- [49] C.-H. Hsu, P. Stano, J. Klinovaja, and D. Loss, Majorana Kramers Pairs in Higher-Order Topological Insulators, *Phys. Rev. Lett.* **121**, 196801 (2018).
- [50] Q. Wang, C.-C. Liu, Y.-M. Lu, and F. Zhang, High-Temperature Majorana Corner States, *Phys. Rev. Lett.* **121**, 186801 (2018).
- [51] Y.-T. Hsu, W. S. Cole, R.-X. Zhang, and J. D. Sau, Inversion-protected higher-order topological superconductivity in monolayer  $\text{WTe}_2$ , *Phys. Rev. Lett.* **125**, 097001 (2020).
- [52] Z. Yan, F. Song, and Z. Wang, Majorana Corner Modes in a High-Temperature Platform, *Phys. Rev. Lett.* **121**, 096803 (2018).
- [53] V. Crépel and L. Fu, New mechanism and exact theory of superconductivity from strong repulsive interaction, *Sci. Adv.* **7**, eabh2233 (2021).
- [54] V. Crépel and L. Fu, Spin-triplet superconductivity from excitonic effect in doped insulators, *Proc. Natl. Acad. Sci. USA* **119**, e2117735119 (2022).
- [55] L.-D. Zhang, F. Yang, and Y. Yao, Possible electric-field-induced superconducting states in doped silicene, *Sci. Rep.* **5**, 8203 (2015).
- [56] Z. Wu, Z. Yan, and W. Huang, Higher-order topological superconductivity: Possible realization in fermi gases and  $\text{Sr}_2\text{RuO}_4$ , *Phys. Rev. B* **99**, 020508(R) (2019).
- [57] X.-H. Pan, K.-J. Yang, L. Chen, G. Xu, C.-X. Liu, and X. Liu, Lattice-Symmetry-Assisted Second-Order Topological Superconductors and Majorana Patterns, *Phys. Rev. Lett.* **123**, 156801 (2019).
- [58] M. Kheirkhah, Y. Nagai, C. Chen, and F. Marsiglio, Majorana corner flat bands in two-dimensional second-order topological superconductors, *Phys. Rev. B* **101**, 104502 (2020).
- [59] Y.-J. Wu, J. Hou, Y.-M. Li, X.-W. Luo, X. Shi, and C. Zhang, In-plane zeeman-field-induced majorana corner and hinge modes in an  $s$ -wave superconductor heterostructure, *Phys. Rev. Lett.* **124**, 227001 (2020).
- [60] K. Laubscher, D. Loss, and J. Klinovaja, Fractional topological superconductivity and parafermion corner states, *Phys. Rev. Res.* **1**, 032017(R) (2019).
- [61] X. Zhu, Tunable majorana corner states in a two-dimensional second-order topological superconductor induced by magnetic fields, *Phys. Rev. B* **97**, 205134 (2018).
- [62] X. Wu, X. Liu, R. Thomale, and C.-X. Liu, High- $T_c$  superconductor  $\text{Fe}(\text{Se},\text{Te})$  monolayer: an intrinsic, scalable and electrically tunable Majorana platform, *Natl. Sci. Rev.* **9**, (2021).
- [63] S.-B. Zhang and B. Trauzettel, Detection of second-order topological superconductors by josephson junctions, *Phys. Rev. Res.* **2**, 012018(R) (2020).
- [64] T. Liu, J. J. He, and F. Nori, Majorana corner states in a two-dimensional magnetic topological insulator on a high-temperature superconductor, *Phys. Rev. B* **98**, 245413 (2018).
- [65] R.-X. Zhang, W. S. Cole, X. Wu, and S. Das Sarma, Higher-Order Topology and Nodal Topological Superconductivity in  $\text{Fe}(\text{Se},\text{Te})$  Heterostructures, *Phys. Rev. Lett.* **123**, 167001 (2019).
- [66] Y. Volpez, D. Loss, and J. Klinovaja, Second-order topological superconductivity in  $\pi$ -junction rashba layers, *Phys. Rev. Lett.* **122**, 126402 (2019).
- [67] M. Kheirkhah, D. Zhu, J. Maciejko, and Z. Yan, Corner- and sublattice-sensitive majorana zero modes on the kagome lattice, *Phys. Rev. B* **106**, 085420 (2022).
- [68] D. Zhu, M. Kheirkhah, and Z. Yan, Sublattice-enriched tunability of bound states in second-order topological insulators and superconductors, *Phys. Rev. B* **107**, 085407 (2023).
- [69] M. Ezawa, Edge-corner correspondence: Boundary-obstructed topological phases with chiral symmetry, *Phys. Rev. B* **102**, 121405(R) (2020).
- [70] E. Khalaf, W. A. Benalcazar, T. L. Hughes, and R. Queiroz, Boundary-obstructed topological phases, *Phys. Rev. Res.* **3**, 013239 (2021).
- [71] A. Tiwari, A. Jahin, and Y. Wang, Chiral dirac superconductors: Second-order and boundary-obstructed topology, *Phys. Rev. Res.* **2**, 043300 (2020).
- [72] X. Wu, W. A. Benalcazar, Y. Li, R. Thomale, C.-X. Liu, and J. Hu, Boundary-Obstructed Topological High- $T_c$  Superconductivity in Iron Pnictides, *Phys. Rev. X* **10**, 041014 (2020).
- [73] K. Asaga and T. Fukui, Boundary-obstructed topological phases of a massive dirac fermion in a magnetic field, *Phys. Rev. B* **102**, 155102 (2020).
- [74] J. Du, T. Li, X. Fan, Q. Zhang, and C. Qiu, Acoustic Realization of Surface-Obstructed Topological Insulators, *Phys. Rev. Lett.* **128**, 224301 (2023).
- [75] K. H. Wong, M. R. Hirsbrunner, J. Gliozzi, A. Malik, B. Bradlyn, T. L. Hughes, and D. K. Morr, Higher order topological superconductivity in magnet-superconductor hybrid systems, [arXiv:2210.15582](https://arxiv.org/abs/2210.15582).
- [76] B.-X. Li and Z. Yan, Boundary topological superconductors, *Phys. Rev. B* **103**, 064512 (2021).
- [77] A. Y. Kitaev, Unpaired majorana fermions in quantum wires, *Phys. Usp.* **44**, 131 (2001).
- [78] W.-F. Tsai, C.-Y. Huang, T.-R. Chang, H. Lin, H.-T. Jeng, and A. Bansil, Gated silicene as a tunable source of nearly 100% spin-polarized electrons, *Nat. Commun.* **4**, 1500 (2013).
- [79] C.-C. Liu, H. Jiang, and Y. Yao, Low-energy effective hamiltonian involving spin-orbit coupling in silicene and two-dimensional germanium and tin, *Phys. Rev. B* **84**, 195430 (2011).
- [80] F. D. M. Haldane, Model for a Quantum Hall Effect without Landau Levels: Condensed-Matter Realization of the “Parity Anomaly”, *Phys. Rev. Lett.* **61**, 2015 (1988).
- [81] C. L. Kane and E. J. Mele,  $Z_2$  Topological Order and the Quantum Spin Hall Effect, *Phys. Rev. Lett.* **95**, 146802 (2005).
- [82] C. L. Kane and E. J. Mele, Quantum Spin Hall Effect in Graphene, *Phys. Rev. Lett.* **95**, 226801 (2005).
- [83] E. Khalaf, Higher-order topological insulators and superconductors protected by inversion symmetry, *Phys. Rev. B* **97**, 205136 (2018).
- [84] R. Jackiw and C. Rebbi, Solitons with fermion number  $1/2$ , *Phys. Rev. D* **13**, 3398 (1976).
- [85] J. Langbehn, Y. Peng, L. Trifunovic, F. von Oppen, and P. W. Brouwer, Reflection-Symmetric Second-Order Topological Insulators and Superconductors, *Phys. Rev. Lett.* **119**, 246401 (2017).
- [86] F. Zhang, C. L. Kane, and E. J. Mele, Topological Mirror Superconductivity, *Phys. Rev. Lett.* **111**, 056403 (2013).
- [87] R. Winkler and H. Deshpande, Effective Hamiltonian for protected edge states in graphene, *Phys. Rev. B* **95**, 235312 (2017).

- [88] P. Delplace, D. Ullmo, and G. Montambaux, Zak phase and the existence of edge states in graphene, *Phys. Rev. B* **84**, 195452 (2011).
- [89] S. Ryu and Y. Hatsugai, Topological Origin of Zero-Energy Edge States in Particle-Hole Symmetric Systems, *Phys. Rev. Lett.* **89**, 077002 (2002).
- [90] A. H. Castro Neto, F. Guinea, N. M. R. Peres, K. S. Novoselov, and A. K. Geim, The electronic properties of graphene, *Rev. Mod. Phys.* **81**, 109 (2009).
- [91] T. Ma, F. Yang, Z. Huang, and H.-Q. Lin, Triplet  $p$ -wave pairing correlation in low-doped zigzag graphene nanoribbons, *Sci. Rep.* **7**, 19 (2017).
- [92] R. C. B. Ribeiro, J. H. Correa, L. S. Ricco, A. C. Seridonio, and M. S. Figueira, Spin-polarized majorana zero modes in double zigzag honeycomb nanoribbons, *Phys. Rev. B* **105**, 205115 (2022).
- [93] R. Verresen, R. Moessner, and F. Pollmann, One-dimensional symmetry protected topological phases and their transitions, *Phys. Rev. B* **96**, 165124 (2017).
- [94] J. C. Budich and E. Ardonne, Topological invariant for generic one-dimensional time-reversal-symmetric superconductors in class DIII, *Phys. Rev. B* **88**, 134523 (2013).
- [95] L. Li, C. Yang, and S. Chen, Topological invariants for phase transition points of one-dimensional  $Z_2$  topological systems, *Eur. Phys. J. B* **89**, 195 (2016).
- [96] Y. Kim, K. Choi, J. Ihm, and H. Jin, Topological domain walls and quantum valley hall effects in silicene, *Phys. Rev. B* **89**, 085429 (2014).
- [97] A. M. Lobos, R. M. Lutchyn, and S. Das Sarma, Interplay of Disorder and Interaction in Majorana Quantum Wires, *Phys. Rev. Lett.* **109**, 146403 (2012).
- [98] M. McGinley, J. Knolle, and A. Nunnenkamp, Robustness of majorana edge modes and topological order: Exact results for the symmetric interacting Kitaev chain with disorder, *Phys. Rev. B* **96**, 241113(R) (2017).
- [99] A. Habibi, S. A. Jafari, and S. Rouhani, Resilience of majorana fermions in the face of disorder, *Phys. Rev. B* **98**, 035142 (2018).
- [100] A. Habibi, R. Ghadimi, and S. A. Jafari, Topological phase diagram of the disordered 2XY model in presence of generalized Dzyaloshinskii–Moriya interaction, *J. Phys.: Condens. Matter* **32**, 015604 (2020).
- [101] S. Gangadharaiah, B. Braunecker, P. Simon, and D. Loss, Majorana Edge States in Interacting One-Dimensional Systems, *Phys. Rev. Lett.* **107**, 036801 (2011).
- [102] R. Ghadimi, T. Sugimoto, and T. Tohyama, Majorana zero-energy mode and fractal structure in fibonacci-kitaev chain, *J. Phys. Soc. Jpn.* **86**, 114707 (2017).
- [103] S. V. Aksenov, A. D. Fedoseev, M. S. Shustin, and A. O. Zlotnikov, Effect of local coulomb interaction on majorana corner modes: Weak and strong correlation limits, *Phys. Rev. B* **107**, 125401 (2023).
- [104] S. C. de la Barrera, S. Aronson, Z. Zheng, K. Watanabe, T. Taniguchi, Q. Ma, P. Jarillo-Herrero, and R. Ashoori, Cascade of isospin phase transitions in bernal-stacked bilayer graphene at zero magnetic field, *Nat. Phys.* **18**, 771 (2022).
- [105] Y.-Z. Chou, F. Wu, J. D. Sau, and S. Das Sarma, Acoustic-phonon-mediated superconductivity in bernal bilayer graphene, *Phys. Rev. B* **105**, L100503 (2022).
- [106] A. L. Szabó and B. Roy, Competing orders and cascade of degeneracy lifting in doped bernal bilayer graphene, *Phys. Rev. B* **105**, L201107 (2022).